

Mössbauer, EPR, and Modeling Study of Iron Trafficking and Regulation in $\Delta ccc1$ and $CCC1$ -up *Saccharomyces cerevisiae*

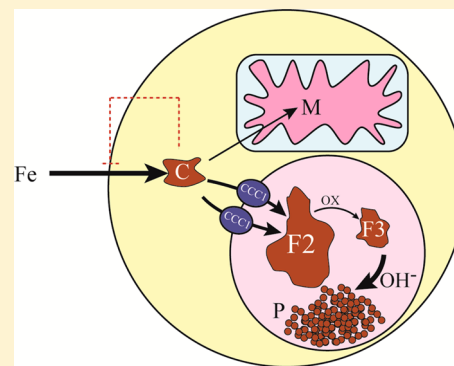
Allison Cockrell,[†] Sean P. McCormick,[‡] Michael J. Moore,[‡] Mrinmoy Chakrabarti,[‡] and Paul A. Lindahl^{*,†,‡}

[†]Department of Biochemistry and Biophysics, Texas A&M University, College Station, Texas 77843-2128, United States

[‡]Department of Chemistry, Texas A&M University, College Station, Texas 77843-3255, United States

S Supporting Information

ABSTRACT: Strains lacking and overexpressing the vacuolar iron (Fe) importer *CCC1* were characterized using Mössbauer and EPR spectroscopies. Vacuolar Fe import is impeded in $\Delta ccc1$ cells and enhanced in *CCC1*-up cells, causing vacuolar Fe in these strains to decline and accumulate, respectively, relative to WT cells. Cytosolic Fe levels should behave oppositely. The Fe content of $\Delta ccc1$ cells grown under low-Fe conditions was similar to that in WT cells. Most Fe was mitochondrial with some nonheme high spin (NHHS) Fe^{II} present. $\Delta ccc1$ cells grown with increasing Fe concentration in the medium contained less total Fe, less vacuolar HS Fe^{III} , and more NHHS Fe^{II} than in comparable WT cells. As the Fe concentration in the growth medium increased, the concentration of HS Fe^{III} in $\Delta ccc1$ cells increased to just 60% of WT levels, while NHHS Fe^{II} increased to twice WT levels, suggesting that the NHHS Fe^{II} was cytosolic. $\Delta ccc1$ cells suffered more oxidative damage than WT cells, suggesting that the accumulated NHHS Fe^{II} promoted Fenton chemistry. The Fe concentration in *CCC1*-up cells was higher than in WT cells; the extra Fe was present as NHHS Fe^{II} and Fe^{III} and as Fe^{III} oxyhydroxide nanoparticles. These cells contained less mitochondrial Fe and exhibited less ROS damage than $\Delta ccc1$ cells. *CCC1*-up cells were adenine-deficient on minimal medium; supplementing with adenine caused a decline of NHHS Fe^{II} suggesting that some of the NHHS Fe^{II} that accumulated in these cells was associated with adenine deficiency rather than the overexpression of *CCC1*. A mathematical model was developed that simulated changes in Fe distributions. Simulations suggested that only a modest proportion of the observed NHHS Fe^{II} in both strains was the cytosolic form of Fe that is sensed by the Fe import regulatory system. The remainder is probably generated by the reduction of the vacuolar NHHS Fe^{III} species.



Iron is a critical component of biological systems, often serving at the active sites of metalloenzymes to promote catalysis. In eukaryotic cells, this redox-active d-block transition metal is found in hemes and other mononuclear centers, iron–sulfur clusters (ISCs), diiron centers, and Fe^{III} oxyhydroxide nanoparticles.^{1,2} Mitochondria are a major site of Fe metabolism in eukaryotic cells. Both ISCs and heme biosynthesis occur in this organelle which houses Fe-rich respiratory complexes.³

In yeast, vacuoles are another major site of Fe metabolism, but their role is not well understood. These acidic organelles store and sequester cellular metabolites, including Fe. They import Fe under Fe-replete growth conditions and export it under Fe-deficient ones.^{4–7} Under Fe-replete growth conditions (defined here as $>10 \mu\text{M}$ Fe^{III} citrate in minimal medium, MM), vacuoles contain *ca.* 3/4th of the Fe contained in fermenting WT cells.⁸ The predominant form of Fe in these organelles is a mononuclear NHHS Fe^{III} species with polyphosphate-related ligands.⁹ Depending on growth and isolation conditions, vacuoles can also contain aggregates of Fe^{III} phosphate- or polyphosphate-associated oxyhydroxide nanoparticles.⁹

Iron enters vacuoles primarily through *Ccc1p*, a protein that localizes on the vacuolar membrane.^{4,10} Some Fe also enters through endocytosis. *CCC1* is tightly regulated through two mechanisms, one of which involves *Yap5p*.¹¹ Under Fe-replete cellular conditions, this Fe-sensing transcription factor is constitutively bound to the *CCC1* promoter which induces transcription of the *CCC1* gene, promoting Fe import into vacuoles. Under low-Fe conditions, *CCC1* expression is down-regulated by *Cth2p*.¹² *CTH2* is a member of the Fe regulon, a collection of *ca.* 25 Fe-associated genes that are controlled by *Aft1p*, an Fe-sensitive transcription factor. Under low-Fe conditions, *Aft1p* localizes to the nucleus where it promotes expression of the Fe regulon and stimulates Fe import. Also under Fe-deficient conditions, *Cth2p* binds and destabilizes *CCC1* mRNA, preventing *Ccc1p* biosynthesis and thus *Ccc1p*-dependent Fe import into vacuoles.¹² Under high-Fe conditions, *Aft1p* localizes to the cytosol where it is inactive, and *Yap5p* dissociates from the *CCC1* promoter.^{11,13} These

Received: January 1, 2014

Revised: April 14, 2014

Published: May 2, 2014

mechanisms collectively regulate Ccc1p-dependent entry of Fe into the vacuole in a manner that appears sensitive to cytosolic Fe.

Vacuoles export Fe to the cytosol during periods of Fe starvation. The proteins involved are homologues of Fe-import proteins on the plasma membrane. Prior to export, vacuolar NHHS Fe^{III} ions are reduced by Fre6p, a ferric reductase.⁷ Reduced Fe^{II} can be exported from the vacuole by the Fet5p/Fth1p complex and by Smf3p, both of which are vacuolar membrane-bound proteins.^{5,6} Fet5p, a multicopper oxidase, and Fth1p, a ferric permease, comprise the high-affinity export system.⁵ The low-affinity system is composed of Smf3p, a divalent metal transport protein which is not specific for Fe.⁶ High-affinity Fe transporters allow cells to grow on medium containing low concentrations of Fe ($[Fe_{med}] < 1 \mu M$).^{14–16} Fre6p, Fet5p, and Fth1p are regulated by Aft1p,^{13,17} whereas Smf3p is regulated by Aft2p, a homologue to Aft1p.^{6,18} When intracellular Fe levels decrease, these vacuolar Fe-export proteins are up-regulated.^{5,13,19} This causes Fe to efflux from the vacuoles and move into the cytosol, probably in the Fe^{II} state.

Vacuoles isolated from cells in which CCC1 is deleted ($\Delta ccc1$) contain ~20% of the Fe typically found in WT vacuoles.⁴ The residual Fe in $\Delta ccc1$ vacuoles is due to Fe uptake via END4-associated endocytosis. The vacuolar Fe concentration in $\Delta end4$ vacuoles (containing functional CCC1) is ~60% of WT levels. Thus, Ccc1p imports 60–80% of vacuolar Fe under Fe-replete WT conditions.

$\Delta ccc1$ cells have difficulty growing in medium containing >3 mM ferrous ammonium sulfate.⁴ Kaplan has proposed that the cytosolic Fe concentration in such cells must be high, arguing that Fe is inhibited from transiting into vacuoles such that it accumulates in the cytosol where it promotes ROS formation.⁴ The Fe concentration in $\Delta ccc1$ cells is low, again consistent with increased cytosolic Fe levels.²⁰

Conversely, when CCC1 is constitutively overexpressed, vacuolar and cellular Fe levels are 3–4 times higher than in WT cells.^{4,7} Kaplan has proposed that in this strain, additional cytosolic Fe is transported to vacuoles, leaving the cytosol Fe-deficient. This activates the Fe regulon which up-regulates Fe-import proteins on the plasma membrane thereby increasing cellular Fe import. Fe import would continue until the sensed Fe species in the cytosol exceeds some threshold concentration. Kaplan hypothesized further that mitochondria and vacuoles share a common cytosolic Fe pool. Evidence for this is that blocking mitochondrial Fe import (by deleting the MRS3 and MRS4 genes which encode the mitochondrial Fe import proteins) increases vacuolar Fe import.^{20,21} We will refer collectively to these as Kaplan's hypotheses.

Mössbauer (MB), EPR, and UV-vis spectroscopies, as well as ICP-MS, were used here to study the Fe content of $\Delta ccc1$ and CCC1-up cells grown under various conditions. Our results qualitatively support Kaplan's hypotheses. Based on these hypotheses, we developed a mathematical model to better quantify these effects. Our results suggest (but do not prove) that the cytosolic Fe complex that is imported into both vacuoles and mitochondria is a mononuclear nonheme high-spin (NHHS) Fe^{II} complex coordinated predominately by O and N donor ligands. They also provide insights regarding the importance of pH and oxidation status in determining the form of Fe in vacuoles.

■ EXPERIMENTAL PROCEDURES

Strains and Growth Conditions. $\Delta ccc1$ and CCC1-up *S. cerevisiae* cells were a generous gift of Jerry Kaplan (University of Utah). Both strains were derived from DY150 (isogenic to W303) as described.¹⁴ WT and $\Delta ccc1$ cells were grown in minimal medium supplemented with 10 μM copper sulfate; the resulting medium will be abbreviated MM. It contained 20% w/v glucose (Fisher Scientific), 5% w/v ammonium sulfate (Fisher Scientific), 1.7 g/L YNB (MP Biomedicals, LLC #4027-112, which lacked ammonium sulfate, ferric citrate, and copper sulfate), 100 mg/L L-leucine (MP Biomedicals, LLC #0219469480), 50 mg/L adenine hemisulfate dehydrate (MP Biomedicals, LLC #0219460790), and 20 mg/L L-histidine (MP Biomedicals, LLC #0210195480). A 40 mM (pH ~ 5) stock of ⁵⁷Ferric citrate (⁵⁷FC) was prepared as described⁸ and added to MM to achieve final concentrations of 1, 10, 20, and 40 μM . The absence of the CCC1 gene in the $\Delta ccc1$ strain was verified by PCR, using primers 5' TTTCGGTCTGGAC-CAATCGC 3' and 5' GCGACCAATGACGAATTAG 3' (Figure S1, B).

The CCC1 gene was overexpressed in CCC1-up cells using a LEU2-marked multicopy plasmid that contained CCC1 under its native promoter.^{4,11} For this reason, leucine was omitted from the medium used to grow CCC1-up cells. Ccc1p overexpression was verified by Western blot analysis of vacuoles isolated from WT and CCC1-up cells. A Ccc1p antibody¹¹ was also provided by Dr. Kaplan.

Sample Preparation for Biophysical Analyses. Cells were grown and prepared as described.⁸ Strains were stored at –80 °C in YAPD medium containing 15% glycerol. Frozen cells were removed with a wooden stick and streaked onto YPAD plates (CCC1-up cells were maintained on YPAD-Leu plates). Single colonies were inoculated into 50 mL of MM and grown for 24 h at 30 °C with shaking. These cells were used to inoculate 1 L of MM. Cultures were grown to an OD₆₀₀ = 1.0 (± 0.1) and harvested. Cells were pelleted (4,000 \times g, 10 min, Sorvall Evolution RC centrifuge, SLC-6000 rotor) and washed 1 \times with 1 mM EGTA and 3 \times with ddH₂O. Cells were packed into MB cups or EPR tubes and frozen in liquid N₂. Alternatively, cells were resuspended in ddH₂O for subsequent UV-vis analysis. Whole cell samples were prepared aerobically. Mitochondria and vacuoles were isolated anaerobically and prepared for spectroscopic analysis as described.^{9,22}

Biophysical Studies. MB, EPR, and UV-vis spectra were collected and analyzed as described.²³ MB spectra were collected using a MS4 WRC spectrometer (SEE Co., Edina MN), calibrated using α -Fe foil at room temperature. Spectra were analyzed and simulated using WMOSS software. EPR spectra were collected at the University of Texas at Arlington on an X-band EMX spectrometer (Bruker Biospin Corp., Billerica, MA) equipped with a bimodal resonator (4116DM) and an Oxford Instruments ESR900 cryostat. Signals were integrated using a custom Matlab (Mathworks.com) program. Spin concentrations were calculated as described²⁴ using 1.00 mM CuSO₄-EDTA as the standard.

UV-vis spectra of whole cells were collected on a Hitachi U3310 spectrometer with a Head-on photomultiplier tube. Spectra were simulated using OriginPro software as described.²³ Packed-cell samples were diluted 3-fold with ddH₂O and analyzed in a 10 mm path length quartz UV-vis cuvette (Precision cells). After collecting MB spectra, isolated mitochondria were thawed anaerobically in a glovebox (≤ 5

Table 1. Summary of Fe Percentages and Concentrations Determined by Biophysical Methods^a

sample	total [Fe] (ICP-MS)	NHHS Fe ^{II} (MB)	HS Fe ^{II} hemes (MB)	CD (MB)	nanoparticles (MB)	NHHS Fe ^{III} (MB)	Fe ^{II} hemes (UV-vis)	g = 4.3 (EPR)
WT1	170 ± 45 μM (6)	25% (43 μM)	5% (9 μM)	60% (103 μM)	<5% (<9 μM)	0%	44 ± 1 μM	0 μM
WT40	490 ± 140 μM (8)	13% (64 μM)	3% (15 μM)	8% (39 μM)	18% (88 μM)	55% (269 μM)	55 ± 3 μM	152 μM
Δ1	148 ± 64 μM (8)	15% (22 μM)	10% (15 μM)	57% (85 μM)	<5% (<7 μM)	0%	46 ± 2 μM	<1 μM
Δ10	209 ± 8 μM (2)	26% (54 μM)	7% (15 μM)	39% (82 μM)	5% (11 μM)	23% (48 μM)	ND	ND
Δ20	285 ± 5 μM (2)	35% (100 μM)	5% (14 μM)	27% (77 μM)	8% (23 μM)	28% (80 μM)	ND	ND
Δ40	360 ± 100 μM (7)	30% (107 μM)	5% (18 μM)	19% (69 μM)	17% (61 μM)	30% (108 μM)	43 ± 4 μM	73 μM
Δ40, Mitos	854 ± 102 μM (2)	37% (316 μM)	5% (43 μM)	32% (273 μM)	23% (197 μM)	0%	364 ± 9 μM	ND
UP1	250 ± 60 μM (3)	51% (130 μM)	3% (10 μM)	10% (30 μM)	19% (50 μM)	18% (50 μM)	32 ± 3 μM	30 μM
UP10	565 ± 10 μM (2)	53% (300 μM)	2% (11 μM)	5% (28 μM)	25% (141 μM)	18% (102 μM)	ND	ND
UP20	979 ± 24 μM (2)	39% (382 μM)	≤1% (≤10 μM)	3% (29 μM)	39% (382 μM)	17% (167 μM)	ND	ND
UP40	1839 ± 750 μM (5)	38% (700 μM)	≤1% (≤18 μM)	2% (37 μM)	24% (441 μM)	17% (313 μM)	31 ± 6 μM	372 μM
UP1+A	385 ± 68 μM (3)	70% (270 μM)	2% (8 μM)	7% (27 μM)	11% (42 μM)	10% (39 μM)	29 ± 3 μM	39 μM
UP40+A	1040 ± 108 μM (4)	18% (187 μM)	2% (21 μM)	4% (42 μM)	29% (301 μM)	45% (468 μM)	40 ± 4 μM	415 μM

^aIn the column “total [Fe]”, the number of replicates are indicated in parentheses. Uncertainties in Mössbauer percentages and corresponding concentrations (in parentheses) are ±3%. Concentrations of Fe^{II} hemes, as determined by UV-vis, are the sum of individual components (hemes *a*, *b*, and *c*), simulated as described.²⁴ The *g* = 4.3 EPR signals were quantified from individual samples (Table S3) as described.²⁴ Sample concentrations were corrected for packing efficiencies: 0.73 for whole cells, 0.75 for isolated vacuoles, and 0.78 for isolated mitochondria.^{9,23,26} ND = not determined.

ppm of O₂, MBraun, Labmaster), diluted 3-fold with SH buffer (0.6 M Sorbitol, 0.02 M HEPES, Fisher Scientific, pH 7.4), and transferred to a 2 mm path length quartz UV-vis cuvette (Precision cells). The cuvette was sealed with a rubber septum and brought out of the glovebox and immediately analyzed by UV-vis.

Metal Concentration Determination. Pellets of whole cells or isolated organelles were prepared for ICP-MS analysis as described.⁹ Briefly, samples (50–100 μL) were digested by adding 100 μL of concentrated trace-metal-grade nitric acid and then heating at 90 °C for ca. 17 h. Samples were diluted to a final volume of 8 mL with high-purity double-distilled-and-deionized (DDDI) water generated using a Teflon sub-boiling still (Saville). Metal concentrations were determined by ICP-MS (Agilent 7700x) utilizing the H₂ reaction mode and detecting ⁵⁷Fe and ⁵⁶Fe.

RESULTS

We used Mössbauer (MB), EPR, and UV-visible spectroscopies to characterize the Fe content of two genetic strains of *S. cerevisiae*, namely *Δccc1* and *CCC1-up*. *Δccc1* cells lack the Cccp1 transporter on the vacuolar membrane, whereas *CCC1-up* cells contain an abundance of this transporter relative to the level found in WT cells. As a result, *Δccc1* cells should contain unusually high concentrations of cytosolic Fe and low concentrations of vacuolar Fe, since cytosolic Fe should be largely unable to move into vacuoles.⁴ Thus, in the MB spectrum of *Δccc1* cells we expected to observe a diminished percentage of the sextet due to vacuolar HS Fe^{III} along with an increased percentage of the feature due to cytosolic Fe. Conversely, we expected that *CCC1-up* cells would contain more vacuolar HS Fe^{III} and less cytosolic Fe. In previous studies, we have been unable to assign features of whole-yeast-cell MB spectra to cytosolic Fe, perhaps due to a low concentration of such species in WT cells. Our initial objective was to evaluate these expectations and be the first to spectroscopically characterize cytosolic Fe in a yeast cell.

WT Cells. The WT strain from which *Δccc1* and *CCC1-up* strains were derived, namely DY150, differed from that used previously by our lab (W303-1B).^{8,25} Thus, we briefly

summarize the Fe content of DY150 to provide a baseline against which *Δccc1* and *CCC1-up* strains can be compared.

Fe concentrations of both WT strains, when grown on MM supplemented with 40 μM FC, were similar (compare Table 1 to Table 1 of ref 8), but the distribution and speciation of Fe were somewhat different. The low-temperature (6 ± 1 K), low-field (0.05 T) MB spectrum of DY150 cells (Figure 1A) was dominated by a sextet due to mononuclear NHHS Fe^{III} species in vacuoles.⁹ The orange line above the spectrum simulates this

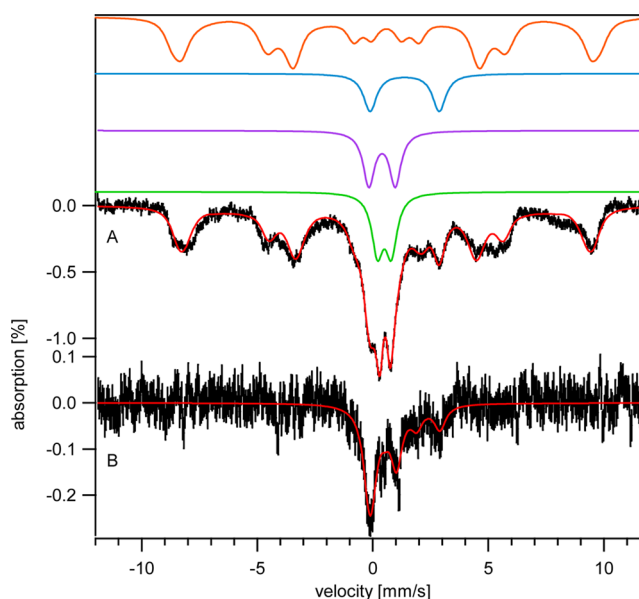


Figure 1. Six K, 0.05 T Mössbauer spectra of DY150 cell grown with [Fe_{med}] = 40 (A) and 1 (B) μM ⁵⁷FC. The orange line simulates NHHS Fe^{III} using *D* = 0.5 cm⁻¹, *E/D* = 0.33, *A₀/γ_{Nβ_N}* = -228 KG, *δ* = 0.54 mm/sec, *ΔE_Q* = 0.39 mm/sec, and *η* = 2. The blue line simulates NHHS Fe^{II} using *δ* = 1.3 mm/s and *ΔE_Q* = 3.0 mm/s. The purple line simulates the CD, using *δ* = 0.45 mm/s and *ΔE_Q* = 1.14 mm/s. The green line simulates Fe^{III} nanoparticles using *δ* = 0.53 mm/s and *ΔE_Q* = 0.45 mm/s. The red lines that overlay the data are composite simulations using percentages in Table 1.

feature. The concentration of Fe associated with it ($\sim 270 \mu\text{M}$) was lower than it was in W303-1B cells ($\sim 380 \mu\text{M}$).⁹ Other components of the DY150 spectrum, including a broad quadrupole doublet arising from superparamagnetic Fe^{III} oxyhydroxide nanoparticles and a doublet arising from one or more NHHS Fe^{II} species, were more intense. The nanoparticle doublet, simulated by the green line in Figure 1, was 4.5 \times more intense than the corresponding doublet in the W303-1B spectrum. The NHHS Fe^{II} doublet, simulated by the blue line in Figure 1, was 1.4 \times more intense. The intensity of the so-called “central doublet” (CD) was similar to that obtained with other strains.²³ The CD originates from $S = 0$ $[\text{Fe}_4\text{S}_4]^{2+}$ clusters and LS Fe^{II} heme centers; the two types of centers cannot be distinguished by MB spectroscopy. The purple line above the spectrum, which simulates the CD, was generated at 8% spectral intensity. The simplest interpretation of these differences is that *ca.* 100 μM of the vacuolar NHHS Fe^{III} species in W303-1B cells was converted into 60 μM of nanoparticles and 40 μM of NHHS Fe^{II} in DY150 cells. This is consistent with vacuoles in DY150 cells being slightly more basic and/or more reducing than vacuoles in W303-1B cells.

The EPR spectrum of DY150 cells grown on MM with 40 μM ^{57}FC (to be called WT40 cells) was dominated by a $g = 4.3$ signal (Figure 2E). This signal arose from a mononuclear,

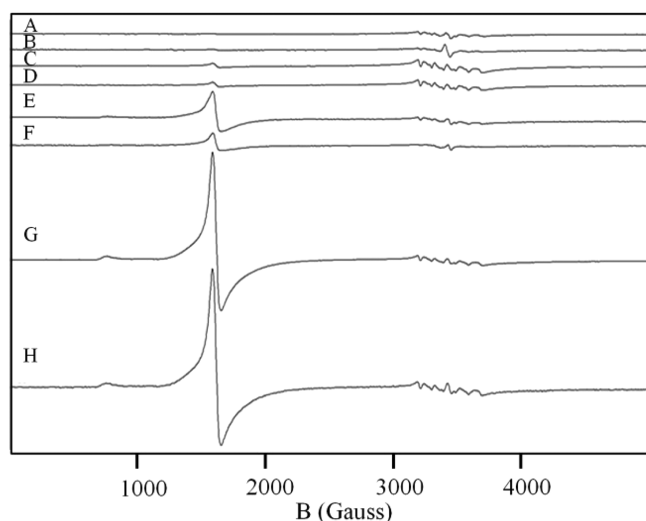


Figure 2. EPR of WT, Δccc1 , and CCC1-up whole cells. A, WT1; B, $\Delta 1$; C, UP1; D, UP1+A; E, WT40; F, $\Delta 40$; G, UP40; H, UP40+A cells. Spectra were collected at 4 K with a microwave frequency of 9.63 GHz and microwave power 0.2 mW.

NHHS Fe^{III} $S = 5/2$ center with rhombic symmetry ($E/D \sim 1/3$),⁹ the same species that afforded the sextet in Figure 1A. The associated EPR concentration was $\sim 150 \mu\text{M}$ (Table 1). This concentration was divided by the cellular Fe concentration ($\sim 350 \mu\text{M}$ for this sample) and by the fraction of the NHHS Fe^{III} sextet in the MB spectrum (0.55) to yield a ratio of 0.8. Given the uncertainties associated with these determinations, we regard this as acceptably near to 1. The $g = 2$ region included a Mn^{II} -based hyperfine-split signal, a low-intensity signal at $g = 2.00$ due to a radical, and a $g_{\text{ave}} = 1.94$ signal due to reduced ISCs. The combined concentration of the last two signals was 2–5 μM .

DY150 cells grown on MM supplemented with 1 μM ^{57}FC (called WT1 cells) contained less Fe than cells grown with 40 μM ^{57}FC (WT40) (Table 1). The low-temperature low-field

MB spectrum of WT1 cells (Figure 1B) was dominated by the CD. HS heme and nonheme Fe^{II} doublets were also evident, as was a minor contribution of nanoparticles. There was no evidence of a NHHS Fe^{III} sextet (though a very low-intensity sextet could be hiding in the noise). WT1 cells did not exhibit a $g = 4.3$ EPR signal (Figure 2A), indicating the absence of NHHS Fe^{III} in the vacuoles of these cells. These results verify a previous study showing that WT1 cells do not accumulate significant Fe in their vacuoles.⁸

Concentrations of Fe^{II} hemes in WT1 and WT40 cells, as determined by UV–vis spectroscopy (Figure 3, A and B; Table

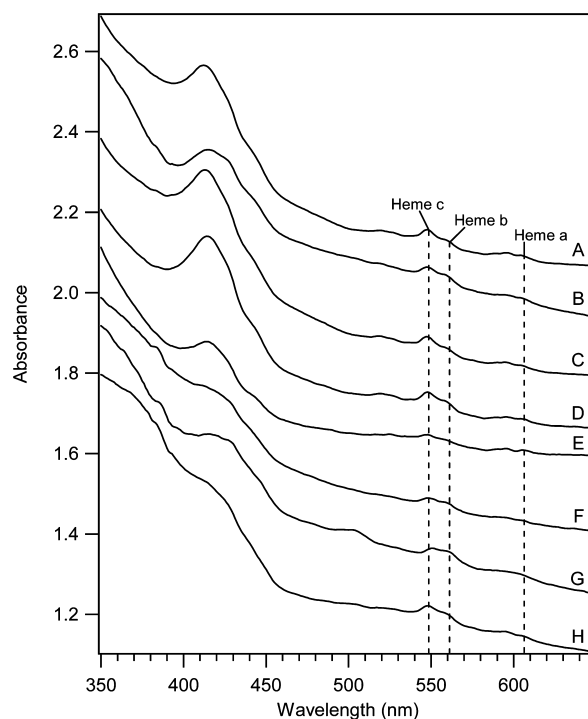


Figure 3. Electronic absorption spectroscopy of WT, Δccc1 , and CCC1-up whole cells. A, WT1; B, WT40; C, $\Delta 1$; D, $\Delta 40$; E, UP1; F, UP40; G, UP1+A; H, UP40+A. Quantifications of individual heme centers are listed in Table S1.

S1), did not change significantly as the medium FC concentration ($[\text{Fe}_{\text{med}}]$) increased. Likewise, the CD and HS Fe^{II} heme concentrations, as determined by MB and ICP-MS, also did not show significant changes. These features are primarily associated with mitochondrial respiratory complexes. Thus, our results indicate similar concentrations of mitochondrial Fe in WT1 and WT40 cells. Since the total Fe content of yeast cells can be roughly decomposed into vacuolar Fe and mitochondrial Fe,^{8,9,26} differences in intracellular Fe concentrations (170 vs. 490 μM) are largely due to differences in vacuolar Fe levels (empty in WT1 cells; *ca.* 300 μM Fe in WT40 cells).

Δccc1 Cells. When grown on MM supplemented with 1, 10, 20, and 40 μM ^{57}FC , these cells will be referred to as $\Delta 1$, $\Delta 10$, $\Delta 20$, and $\Delta 40$, respectively. The Fe concentrations in these cells were $\sim 20\%$ less than in the corresponding WT cells (Table 1).

The low-temperature low-field MB spectrum of $\Delta 1$ cells (Figure 4A) was dominated by the CD. Although the spectrum was noisy, doublets due to HS nonheme and heme Fe^{II} could be discerned; the red line is a composite simulation using

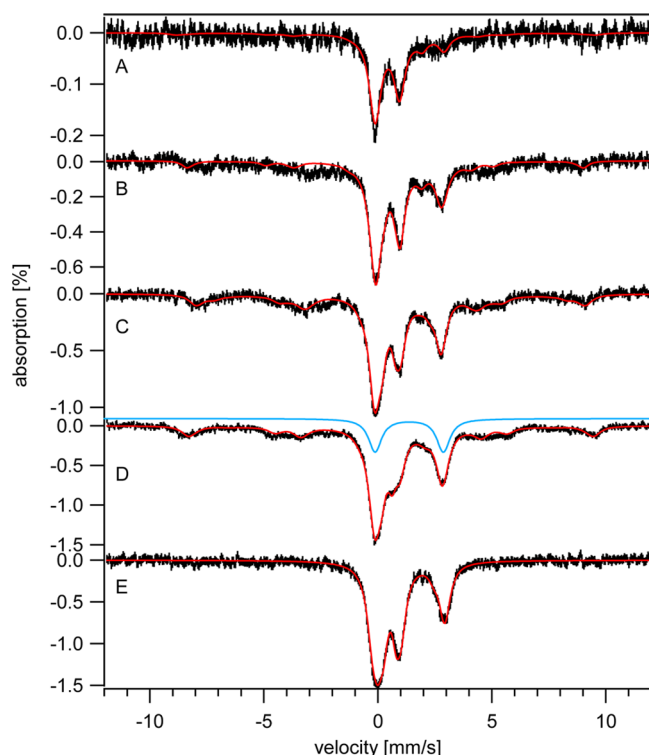


Figure 4. Five K, 0.05 T Mössbauer spectra of $\Delta ccc1$ cells and isolated mitochondria. A, $\Delta 1$ cells; B, $\Delta 10$ cells; C, $\Delta 20$ cells; D, $\Delta 40$ cells; E, mitochondria isolated from $\Delta 40$ cells. Red lines are simulations of the entire spectrum using the percentages given in Table 1. The blue line is a simulation of the NHHS Fe^{II} feature generated with parameters specified in Figure 1.

percentages given in Table 1. EPR of $\Delta 1$ cells (Figure 2B) did not exhibit a $g = 4.3$ signal, consistent with the MB spectrum which lacked the corresponding sextet. UV–vis spectra of $\Delta 1$ cells (Figure 3C) showed that the concentrations of reduced hemes in $\Delta 1$ cells were similar to those in WT1 cells. These results indicated that *under low-Fe conditions, the absence of CCC1 had no significant effect on cellular Fe content, relative to WT cells grown under similar conditions.* This makes sense because vacuoles do not store Fe under low-Fe conditions, and so the absence of the vacuolar Fe importer should be largely irrelevant under these conditions.

The MB spectra of $\Delta 10$, $\Delta 20$, and $\Delta 40$ cells (Figure 4, B, C and D) exhibited less CD on a percentage basis than was evident in the $\Delta 1$ spectrum, but the absolute concentrations of CD-associated Fe were all similar (Table 1). The concentration of HS Fe^{II} hemes also remained relatively constant as $[\text{Fe}_{\text{med}}]$ increased. The total concentrations of reduced hemes in $\Delta 1$ and $\Delta 40$ cells, as monitored by UV–vis (Figure 3, C and D), were similar to each other ($40\text{--}50\text{ }\mu\text{M}$) and to those in analogous WT cells (Figure 3, A and B). These results indicate that *the concentrations of Fe-containing centers in the mitochondria of $\Delta ccc1$ and WT cells were similar and were largely unaffected by changes in $[\text{Fe}_{\text{med}}]$.*

The major changes occurring in the MB spectra of $\Delta ccc1$ cells prepared with increasing $[\text{Fe}_{\text{med}}]$ were lower-than-normal increases in the sextet associated with vacuolar NHHS Fe^{III} and greater-than-normal increases in the NHHS Fe^{II} doublet (Figure 4, B – D, and Table 1). The concentration of vacuolar Fe^{III} increased to only $\sim 110\text{ }\mu\text{M}$ in $\Delta 40$ cells. This was less than half of that in WT40 cells. Confirming this, $\Delta 40$ cells

exhibited a $g = 4.3$ EPR signal (Figure 2F) that was also about half as intense as exhibited by WT40 cells (Figure 2E). This implies that $\sim 60\%$ of vacuolar Fe in WT40 cells is imported via Ccc1p; the remaining vacuolar Fe (evident in $\Delta 40$ vacuoles) must enter through other pathways (e.g., END4-associated). Interestingly, the resulting vacuolar Fe in $\Delta 40$ cells exhibited the same spectroscopic signature as in WT cells, implying the same structure (i.e., a mononuclear NHHS Fe^{III} complex with polyphosphate-related ligands) regardless of whether the Fe is imported via Ccc1p or another pathway.

What happened to the other half of the Fe in $\Delta 40$ cells that, in WT40 cells, is imported into vacuoles via Ccc1p? We hypothesize that this Fe gives rise to some of the intensity associated with the NHHS Fe^{II} doublet simulated by the blue line in Figure 4D. The concentration associated with this feature in $\Delta 40$ cells increased from $20 \rightarrow 110\text{ }\mu\text{M}$ as $[\text{Fe}_{\text{med}}]$ increased. This represents about twice the concentration observed in corresponding WT cells (compare the blue doublet line of Figure 4D to that of 1A). Moreover, this species accumulated in the range of $[\text{Fe}_{\text{med}}]$ normally associated with the import of Fe into the vacuoles ($10\text{--}40\text{ }\mu\text{M}$).

We initially conjectured that the NHHS Fe^{II} doublet in MB spectra of $\Delta ccc1$ cells represented a single cytosolic Fe complex that in WT cells enters vacuoles via the Ccc1p-dependent import pathway. Since the Fe concentration in $\Delta ccc1$ cells was $\sim 20\%$ less than in equivalent WT cells, we further conjectured that this putative cytosolic Fe^{II} complex was sensed by the system that regulates Fe import into the cell. Accordingly, its higher concentration in $\Delta ccc1$ cells would down-regulate Fe import, as observed. We also found that $\Delta 40$ cells suffered ~ 4 times more oxidative damage than comparable WT cells (Figure S2). This is consistent with the idea that the putative cytosolic NHHS Fe^{II} complex, in higher-than-WT levels, promoted Fenton chemistry which caused the increased oxidative damage. As described below, our modeling studies suggest that only a modest portion of the ions giving rise to the NHHS Fe^{II} doublet is actually due to the sought-after cytosolic Fe species. The remainder appears to be a different NHHS Fe^{II} species - different either structurally or in its location (perhaps it is located in vacuoles rather than in cytosol).

The Fe concentration in mitochondria isolated from $\Delta 40$ cells ($\sim 860\text{ }\mu\text{M}$) was slightly higher than that in W303-1B mitochondria ($\sim 710\text{ }\mu\text{M}$).^{8,23,26} Heme signals in the UV–visible spectra of mitochondria from $\Delta 40$ cells were also more intense (Figure S3). The same primary MB features were observed in WT cells, including the CD, a NHHS Fe^{II} doublet, a nanoparticle doublet, and a doublet due to HS Fe^{II} hemes (Figure 4E). Spectral intensities were also similar to those of WT mitochondria except that the NHHS Fe^{II} doublet was more intense. The increased Fe levels in $\Delta 40$ mitochondria probably arose from a higher rate of mitochondrial Fe import due in turn to a higher concentration of cytosolic Fe. The modest increase in mitochondrial NHHS Fe^{II} is insufficient to account for the high concentration of NHHS Fe^{II} observed in whole $\Delta 40$ cells—most of these ions are nonmitochondrial.

CCC1-up Cells. Western blot analysis of vacuoles isolated from CCC1-up cells grown with $40\text{ }\mu\text{M}$ FC (abbreviated UP40 cells) showed that these organelles contained approximately twice the concentration of Ccc1p as found in WT40 vacuoles (Figure S1, A). A similar relative level of Ccc1p abundance was assumed for all CCC1-up cells, regardless of medium Fe concentration.

The concentration of Fe in CCC1-up cells grown with 1 μM FC in the medium (called "UP1" cells) was substantially higher than that in WT1 cells (Table 1). The low-temperature low-field MB spectrum of UP1 cells was dominated by a NHHS Fe^{II} doublet (Figure 5A). This feature was more intense than it was

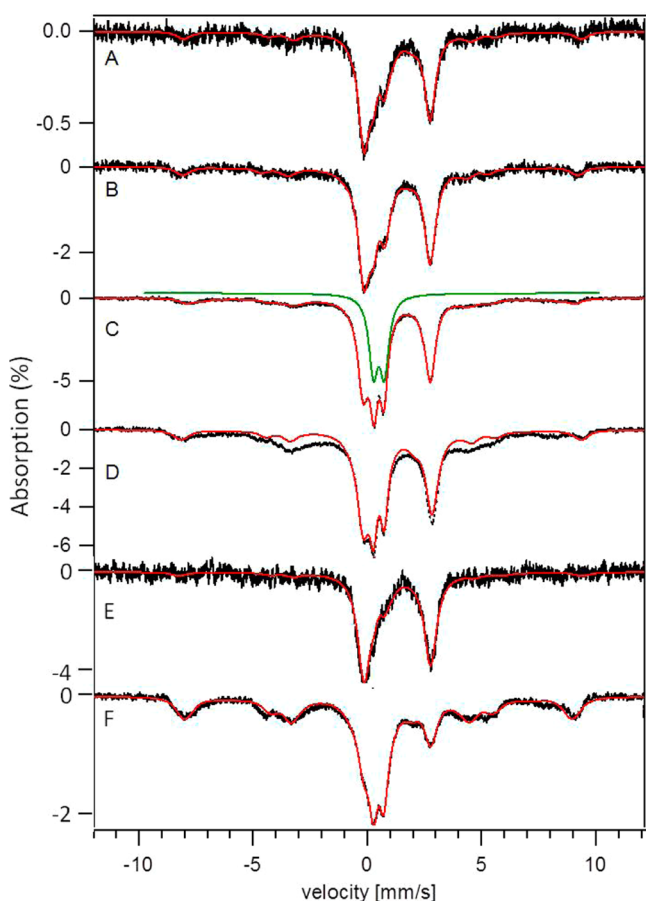


Figure 5. Five K, 0.05 T Mössbauer spectra of CCC1-up cells grown at various FC concentrations. A, UP1; B, UP10; C, UP20; D, UP40; E, UP1+A; F, UP40+A. The red lines are simulations of the entire spectrum using the percentages in Table 1. The green line is a simulation of the nanoparticle feature generated using parameters specified in Figure 1.

in spectra of WT1 or $\Delta 1$ cells, corresponding to 130 μM Fe^{II} in UP1 vs 43 μM in WT1 vs 22 μM in $\Delta 1$. The sextet and doublet due to NHHS Fe^{III} and nanoparticles, respectively, were also somewhat more noticeable (compare Figure 5A to Figures 1B and 4A). The intensity of the $g = 4.3$ EPR signal exhibited by UP1 cells was slightly higher (compare Figure 2C to A and B; also see Table 1).

The dominance of the NHHS Fe^{II} doublet in the MB spectrum of UP1 cells diminished our ability to quantify the intensity of the CD. However, after removing the contributions of the NHHS Fe^{II} doublet, the NHHS Fe^{III} sextet, and the nanoparticle doublet, little intensity remained that could be fitted to the CD. Consistent with this, the UV-vis spectrum of UP1 cells (Figure 3E) indicated a lower concentration of Fe^{II} hemes (mostly mitochondrially associated) in UP1 cells, relative to in WT1 (Figure 3A) or $\Delta 1$ cells (Figure 3C). Collectively, these results indicated that the concentration of mitochondrial Fe was lower in UP1 cells than in WT1 or $\Delta 1$

cells, while the concentrations of vacuolar HS Fe^{III} and the NHHS Fe^{II} species were higher.

The concentration of Fe in UP10 cells was about twice that in UP1 cells. The low-temperature low-field MB spectrum of UP10 cells (Figure 5B) was similar to that of UP1 cells, with the NHHS Fe^{II} doublet again dominating. The NHHS Fe^{III} sextet was evident, as was a shoulder on the low-energy doublet line due to nanoparticles. The intensity of the CD was again low, corresponding to an Fe concentration of $\sim 30 \mu\text{M}$. Low concentrations of CD-associated Fe were also present in UP20 and UP40 cells.

The Fe concentration in UP20 cells was nearly twice that in UP10 cells, and the associated MB spectrum (Figure 5C) was correspondingly more intense. The NHHS Fe^{II} doublet remained intense but was slightly diminished on a percentage-wise basis than in UP1 or UP10 spectra. The intensity of the nanoparticle doublet (Figure 5C, highlighted by the green line simulation) was more than twice that in UP10 cells. The concentration of the NHHS Fe^{III} species was also increased (Table 1).

The Fe concentration of UP40 cells was nearly twice that of UP20 cells (Table 1). Such a proportional increase in the cellular Fe concentration of UP cells with increasing $[\text{Fe}]_{\text{med}}$ (doubling from $[\text{Fe}]_{\text{med}} = 10 \mu\text{M} \rightarrow 20 \mu\text{M}$, and doubling again from $[\text{Fe}]_{\text{med}} = 20 \mu\text{M} \rightarrow 40 \mu\text{M}$) is unusual. It indicates that import of Fe into CCC1-up cells is effectively unregulated. A component of the regulatory machinery could be defective in UP cells, but we find it more likely that the concentration of the sensed cytosolic Fe species used in regulating Fe import was significantly below the threshold concentration in CCC1-up cells, even when grown on $[\text{Fe}]_{\text{med}}$ as high as 40 μM Fe. Given that these cells contained a high concentration of NHHS Fe^{II} , these considerations again suggested that only a portion of the observed NHHS Fe^{II} species was sensed by the cytosolic regulatory system.

The low-temperature low-field MB spectrum of UP40 cells was again dominated by the NHHS Fe^{II} doublet (Figure 5D). In fact, the NHHS Fe^{II} concentration in UP40 cells was the highest observed in this study. Curiously, Oxyblot analysis revealed that these cells exhibited less ROS damage than did Δccc1 cells (Figure S2). This raised the possibility that the majority of NHHS Fe^{II} in UP cells might, for some reason, be unable to promote Fenton chemistry. A substantial proportion of the NHHS Fe^{II} observed in UP cells may be located in vacuoles where they might not generate ROS as readily as NHHS Fe^{II} in other cellular compartments (e.g., the cytosol). Inconsistent with this, vacuoles isolated from UP40 cells did not exhibit an intense NHHS Fe^{II} doublet; most Fe was present as nanoparticles (Figure S4). However, NHHS Fe^{II} may have leached out of the organelle during isolation.

The UP40 spectrum exhibited a strong nanoparticle doublet, similar to that exhibited by UP20 cells, and a more intense NHHS Fe^{III} sextet relative to that in the UP20 spectrum. Consistent with this, EPR of UP40 cells showed an intense $g = 4.3$ signal representing $\sim 370 \mu\text{M}$ HS Fe^{III} (Figure 2G and Table S2). The ratio of the EPR-based concentration to the Mössbauer-based HS Fe^{III} concentration was 0.9 which was within error of unity.

After contributions from the 3 dominant features in the MB spectrum of UP40 cells had been simulated and subtracted, a portion of the remaining MB spectral intensity could be fitted to the CD and the HS Fe^{II} heme doublet. However, the associated concentrations were low (Table 1). UV-vis analysis

revealed that the levels of Fe^{II} hemes were similarly low in UP1 and UP40 cells (Figure 3, E and F; Table 1). Viewed collectively, our analysis indicates that mitochondrial Fe levels were low in UP cells, despite the elevated intracellular Fe concentrations. This makes sense: when *Ccc1p* is overexpressed, less than the normal amount of Fe is trafficked into mitochondria because of lower cytosolic Fe concentrations. Consistent with this, the Fe concentration in mitochondria isolated from UP40 cells (460 μ M) was lower than in mitochondria from WT40 cells (700–800 μ M). MB spectra of UP40 mitochondria indicated normal (WT40) percentages of NHHS Fe^{II}, the CD, and nanoparticles (Figure S5).

The 5 K MB spectrum of UP40 cells also exhibited a broad, magnetic feature that accounted for ~15% of spectral intensity, corresponding to ~280 μ M Fe. At 100 K this feature collapsed and the intensity in the central region of the MB spectrum increased. Variable-temperature EPR of UP40 cells showed a broad signal in the $g = 2$ region which displayed anti-Curie Law behavior. The product of signal-intensity \times temperature (Figure 6) was 5-times more intense at 78 K (black line)

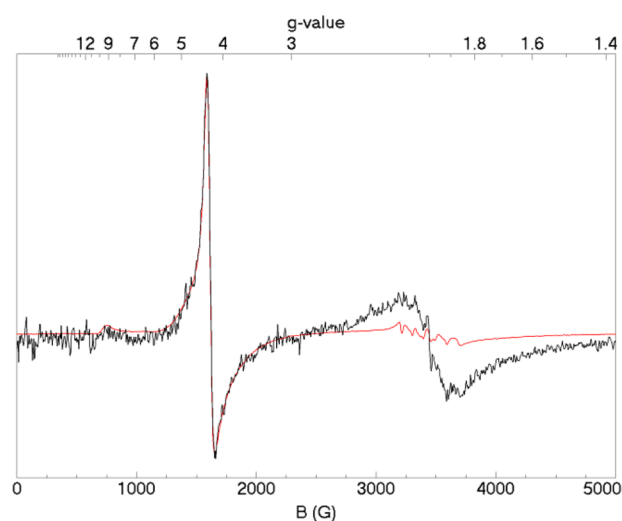


Figure 6. Variable temperature EPR spectra of UP40 cells. The red spectrum was collected at 10 K; the black spectrum at 79 K. Spectra were collected using microwave frequency 9.63 GHz and microwave power 0.2 mW. Spectra were normalized and plotted using SpinCount software (<http://www.chem.cmu.edu/groups/hendrich>).

than it was at 10 K (red line). In these spectra, the $g = 4.3$ signal intensity, which followed the Curie Law, served as a control and was of equal intensity in both plots. Similar features have been observed in spectra of other Fe-overloaded yeast cells.²⁷ The origin of these features remain unestablished, but we suspect a distinct form of nanoparticles relative to those that exhibit a broad doublet at 5 K.^{28,29}

Adenine Deficiency of *CCC1-up* Cells. When UP cells reached an OD₆₀₀ ~1.0, a pink color was observed which indicates an adenine deficiency.³⁰ Standard MM, containing 50 mg L⁻¹ of adenine, is sufficient to suppress this phenotype in WT cells, but lowering the adenine concentration in the growth medium 8-fold causes an adenine deficiency (Park and Lindahl, unpublished). Park and Lindahl (unpublished) discovered that Fe in adenine-deficient WT cells is dominated by NHHS Fe^{II} and argued that the vacuoles in such cells are more reducing than those in adenine-replete WT cells. This difference causes NHHS Fe^{III} ions in the organelle to become reduced. The pink

color and high concentration of NHHS Fe^{II} in UP40 cells indicated that these cells are adenine-deficient in medium that is sufficient to prevent adenine deficiency in WT cells.

We wondered whether some (or all) of the Fe-associated phenotype that we had presumed to be linked directly with the overexpression of *Ccc1p* might actually be more closely associated with adenine deficiency. To deconvolute these factors, we sought to relieve the adenine deficiency of *CCC1-up* cells by growing them on MM containing twice the normal adenine concentration. Indeed the resulting UP1+A cells did not turn pink. The concentration of Fe in UP1+A cells was slightly higher than in UP1 cells, but the corresponding MB spectra (Figure 5, E vs. A) were similar in that both were dominated by the NHHS Fe^{II} doublet. EPR spectra were also similar (Figures 2, D vs. C). Corresponding UV-vis spectra were fairly similar (Figure 3, G vs. E), but the heme intensities in the UP1 spectrum were lower than in UP1+A spectrum. Viewed collectively, these results indicate that under low-Fe growth conditions, the observed buildup of NHHS Fe^{II} is due primarily to *CCC1* overexpression rather than to adenine deficiency.

The situation was different under high-Fe conditions. Again, UP40+A cells did not develop a pink color, but their Fe-related phenotype differed relative to that of UP40 cells. UP40+A cells contained about half as much Fe as UP40 cells (Table 1), with less NHHS Fe^{II} and more NHHS Fe^{III} and nanoparticles. These differences afforded a MB spectrum (Figure 5F) that was reminiscent of the WT40 spectrum (Figure 1A). The concentrations of Fe species associated with mitochondria, including the CD (Figure 5F) and heme centers (Figure 3H) were not noticeably affected by relieving the adenine deficiency. Like UP40 cells, UP40+A cells exhibited a broad $g = 2$ feature by EPR which displayed anti-Curie law behavior (Figure S6).

Despite the lower cellular Fe concentration, UP40+A cells exhibited a $g = 4.3$ EPR signal (Figure 2H) that had a slightly higher spin concentration than that of UP40 cells. This confirmed a shift from mononuclear NHHS Fe^{II} \rightarrow Fe^{III} as UP40 cells were relieved of their adenine deficiency. Although not evident from the EPR, some NHHS Fe^{II} also shifted to Fe^{III} nanoparticles. These differences imply that ~75% of the NHHS Fe^{II} species that accumulated in UP40 cells are more closely associated with adenine deficiency than *CCC1* overexpression.

That the loss of this NHHS Fe^{II} resulted in a decline in the concentration of cellular Fe sparked an insight. If the lost NHHS Fe^{II} were the sensed form of Fe in the cytosol, its decline should have been associated with an increase in cellular Fe. Since the opposite happened, we realized that most of the NHHS Fe^{II} species present in *CCC1-up* cells must not be sensed by the Fe-import regulatory system.

Manganese Homeostasis. Although not the focus of this paper, some effects involving Mn are relevant to understanding the effects of $\Delta ccc1$ and *CCC1-up* on Fe metabolism. The $g = 2$ regions of the WT1 and WT40 EPR spectra (Figure 2, A and E) were dominated by a Mn^{II}-based hyperfine-split signal, quantifying in both spectra to a spin concentration of ~35 μ M (Table S2). This concentration was normalized to the cellular Mn concentration, yielding a [spin]/[Mn] ratio of 0.9. This confirms a previous report that the vast majority of the Mn in yeast cells is EPR-active,⁸ and it demonstrates that the cellular Mn concentration is not affected by different concentrations of Fe in the growth medium.

$\Delta ccc1$ cells exhibited similar Mn^{II}-based signals (Figure 2, B and F), but spin concentrations were lower (<10 μ M). This

correlated to a lower Mn concentration in these cells ($\sim 16 \mu\text{M}$, Table S2). In contrast, the concentration of Mn in *CCC1-up* cells was $\sim 80 \mu\text{M}$ (averaging values for UP1, UP40, UP1+A, and UP40+A cells), which was double the concentration of Mn in WT cells and about 5 times the concentration in Δccc1 cells. These results are consistent with reports that cellular Mn is elevated when *CCC1* is overexpressed.⁴ The intensity of the Mn^{II} signal in the EPR spectrum of UP1 cells (Figure 2C) was also greater than in WT1 (Figure 2A) or $\Delta 1$ (Figure 2B) cells, affording a $[\text{spin}]/[\text{Mn}]$ ratio of ~ 0.9 . Again, this indicates that the vast majority of Mn in UP1 cells is mononuclear Mn^{II} and EPR-active. The Mn^{II} EPR signal intensities exhibited by UP1, UP40, and UP40+A cells were similar (Table S2). This indicates that the Mn^{II} levels are not affected by adenine supplementation or by variations in $[\text{Fe}_{\text{med}}]$.

Besides transporting Fe into vacuoles, *Ccc1p* also transports Mn^{II} ions.³¹ Therefore, the same argument that was used to explain the variations in Fe concentrations in Δccc1 and *CCC1-up* cells can also explain the variation in Mn concentrations. Accordingly, when *Ccc1p* is absent, cytosolic Mn^{II} ions cannot enter vacuoles as rapidly, so they accumulate in the cytosol. The cytosolic Mn-regulatory system senses this and shuts-down further Mn import into the cell. This is why the Mn concentration in Δccc1 cells was low. When *CCC1* is overexpressed, cytosolic Mn^{II} enters vacuoles at a faster-than-normal rate, leaving the cytosol Mn-deficient. The regulatory machinery senses this low cytosolic Mn concentration and increases the import flux of Mn, leading to the observed higher Mn concentration in *CCC1-up* cells.

Mathematical Model. Kaplan's hypotheses provide a conceptual framework to understand our results, but we wanted to explore these hypotheses more quantitatively. To do this, we developed a simple deterministic mathematical model involving ordinary differential equations (ODEs). The model represents an explicit hypothesis regarding the mechanism of Fe trafficking and homeostasis in WT, Δccc1 and *CCC1-up* cells, as illustrated in Figure 7. It posits that cellular Fe is composed of 5 components

$$[\text{Fe}_{\text{cell}}] = [\text{F3}] + [\text{P}] + [\text{M}] + [\text{C}] + [\text{F2}] \text{ and } \frac{d[\text{Fe}_{\text{cell}}]}{dt} = \frac{d[\text{F3}]}{dt} + \frac{d[\text{P}]}{dt} + \frac{d[\text{M}]}{dt} + \frac{d[\text{C}]}{dt} + \frac{d[\text{F2}]}{dt}$$

Component F3 was assigned to the NHHS Fe^{III} species located in vacuoles. P was assigned to Fe^{III} oxyhydroxide nanoparticles. M was "mitochondrial Fe", taken for simplicity to be the sum of the MB central doublet, due mainly to $[\text{Fe}_4\text{S}_4]^{2+}$ clusters, and the Fe^{II} heme centers, as observed by UV-vis. Most of these centers in the cell are present in mitochondrial respiratory complexes. In the model, [M] was influenced by the import of Fe from the cytosol and the dilution of M by cell growth.

A tenet of Kaplan's hypotheses is that yeast cells contain a single cytosolic Fe species that is imported through the plasma membrane and exported into both mitochondria and vacuoles. In our model, C was assigned to this species. Accordingly, [C] was determined by the balance of these processes. For a growing cell, increasing volume would also diminish the concentration of C by dilution. These four processes are included in the ODE $d[\text{C}]/(dt = k_{\text{in}} \cdot \text{nut} - k_{\text{m}} \cdot [\text{C}] - k_{\text{ccc1}} \cdot [\text{C}] - \alpha \cdot [\text{C}])$. Here k_{in} is the apparent first-order rate-constant associated with the import of Fe through the plasma membrane, and *nut* is the concentration of nutrient Fe in the

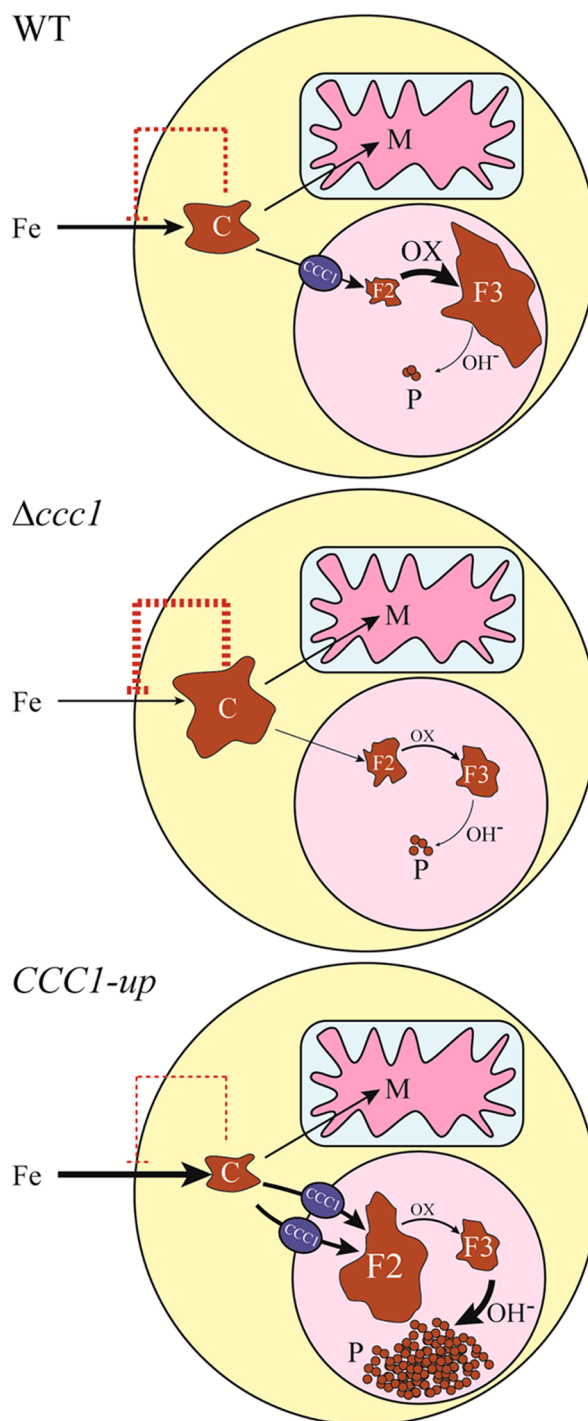


Figure 7. Models of Fe trafficking in WT, Δccc1 , and *CCC1-up* cells. In WT cells, Fe import is regulated by the concentration of cytosolic Fe C. Mitochondria and vacuoles compete to import C. The majority of C enters the vacuoles via *Ccc1p*. Once in the vacuole, vacuolar iron F2 is oxidized to HS Fe^{III} (F3); at high pH, a portion of this Fe is converted into nanoparticles P. In Δccc1 cells, there is no *Ccc1p*-dependent Fe influx into vacuoles, so cytosolic Fe increases in concentration. This concentration exceeds a threshold value such that further import into the cell is inhibited. In *CCC1-up* cells, overexpression of *CCC1* increases the flux of Fe into the vacuole, thereby decreasing the concentration of cytosolic Fe below a threshold value, such that Fe import into the cell is upregulated.

medium, presumed to have a first-order dependence on the Fe import rate. The second term of the ODE describes the rate of

Fe import into the mitochondria, which is presumed to be proportional to rate-constant k_m and the concentration of C . The third ODE term describes the rate by which C is imported into vacuoles, assumed to be proportional to the product of k_{cc1} and $[C]$. The apparent first-order rate-constant k_{cc1} should be viewed as the product of an intrinsic rate-constant multiplied by the concentration of $Ccc1p$ on the vacuolar membrane. Thus, k_{cc1} will be different for each genetic strain. The last term of the ODE reflects the dilution of C due to cell growth. Here α is the apparent first-order rate-constant associated with the growth rate of the cell. This parameter was assumed to equal the inverse of the doubling-time ($\alpha = 1/DT = 0.5 \text{ h}^{-1}$).

We initially assumed that C referred to the species corresponding to the entire NHHS Fe^{II} doublet observed by MB spectroscopy but were unable to construct a viable model based on this assumption. We then assumed that the NHHS Fe^{II} doublet arose from two cellular species, namely C and $F2$. That two NHHS Fe^{II} species might yield indistinguishable quadrupole doublets is neither unreasonable nor remarkable. Numerous mononuclear NHHS Fe^{II} complexes afford a doublet with the observed parameters, which merely indicate that the Fe is 5- or 6-coordinate with primarily O/N donors.

The locations of $F2$ and nanoparticles (referred to as P in our model) are uncertain. Neither appears to be located in mitochondria, but they might be located in vacuoles or cytosol. In our model, $F2$ is presumed to be located in vacuoles, which implies the relationship $C \rightarrow F2 \rightarrow F3$. This is chemically simpler than $C \rightarrow F3 \rightarrow F2$. These considerations are reflected in the ODE $d[F2]/dt = k_{cc1} \cdot [C] - k_{23} \cdot [F2] - \alpha \cdot [F2]$. The first term describes the increase in $[F2]$ as C is imported from the cytosol. The second reflects the conversion of $F2 \rightarrow F3$. k_{23} is the apparent first-order rate-constant for this process, with $F2$ assumed to have a first-order dependence. The third term describes the dilution of $F2$ due to cell growth. For nanoparticles P , we assumed the connectivity $F3 \rightarrow P$ and that this reaction occurred in vacuoles. The rate-constant k_{np} is associated with the $F3 \rightarrow P$ reaction and is sensitive to the pH of the vacuoles, with greater values corresponding to higher pH. The ODE that describes the change in the concentration of $F3$ is $d[F3]/dt = k_{23} \cdot [F2] - k_{np}[F3] - \alpha \cdot [F3]$.

In its current form, the trafficking processes included in the model could not mimic the observed changes in cellular Fe as $[\text{Fe}_{\text{med}}]$ changed. To correct this, regulation had to be included. Since the molecular-level details of the Fe regulatory system are not well understood, we used the Reg_- and Reg_+ functions as surrogates.²⁷

$$\text{Reg}_-(F_e, K_s, ns) = \frac{1}{1 + \left(\frac{[F_e]}{K_s}\right)^{ns}}$$

can be viewed as a “valve” that homeostatically regulates the flow of Fe. The valve is half-opened when the concentration of the sensed form of Fe, called F_e , equals some threshold concentration K_s . When $[F_e] > K_s$, flow decreases; when $[F_e] < K_s$, flow increases. The sensitivity of this effect is dictated by the exponent ns which is typically ≥ 1 . The Reg_+ function ($\text{Reg}_+ = 1 - \text{Reg}_-$) behaves oppositely.

A Reg_- valve was used to regulate cellular Fe import. We presumed that cytosolic Fe C was sensed by the system. $[C]$ should be higher than threshold value K_c in $\Delta ccc1$ cells, lower than K_c in $CCC1\text{-up}$ cells, and roughly equal to K_c in WT cells grown under standard conditions (ca. $1\text{--}10 \mu\text{M}$).

Cth2p and Yap5p regulate vacuolar Fe import (see *Introduction*) such that Fe is imported into vacuoles only as $[C]$ increases. To mimic this, we augmented the rate of Fe import into the vacuole with the $\text{Reg}_+(C, K_{v1}, nv1)$ function. This arrangement worked well for cells grown at low $[\text{Fe}_{\text{med}}]$ but not for cells grown at high $[\text{Fe}_{\text{med}}]$, in that too much Fe was imported into vacuoles relative to what was observed. Thus, we augmented the same term with a Reg_- function in which $F3$ was the sensed form of Fe. The product $\{\text{Reg}_+(C, K_{v1}, nv1) \cdot \text{Reg}_-(F3, K_{v2}, nv2)\}$ allowed Fe into the vacuole as $[\text{Fe}_{\text{med}}]$ increased but limited the extent of Fe import for cells grown on high $[\text{Fe}_{\text{med}}]$.

The regulation of Fe import into mitochondria is not well-defined. The prevailing view is that this process is regulated by the ISC biosynthesis activity in mitochondria, with the inner-membrane-bound Atm1p exporting a S-containing species which integrates into the $\text{Grx}/\text{Fra}/\text{Aft1}$ pathway.^{3,32–34} Despite excellent progress in establishing the roles of $\text{Aft1}/2p$,^{13,35,36} Yap5p ,^{11,37,38} $\text{Cth1}/2p$,^{12,39} $\text{Mrs3}/4p$,^{40,41} $\text{Grx3}/4p$,^{35,42–44} and $\text{Fra1}/2p$,^{33,45} the details of the pathway are insufficiently understood to be modeled mathematically. Models that included the product $\{\text{Reg}_-(C, K_{m1}, nm1) \cdot \text{Reg}_-(M, K_{m2}, nm2)\}$ fit the data best. One Reg_- function was sensitive to cytosolic Fe C and the other to mitochondrial Fe M . Relating this to the prevailing perspective, the rate of Atm1 -dependent export of the S-species may be sensitive to ISC biosynthesis (modeled by the Reg_- function sensing M); while the rate by which that species is used to assemble the $[\text{Fe}_2\text{S}_2]$ cluster associated with the $\text{Grx}/\text{Fra}/\text{Aft1}$ pathway may be sensitive to cytosolic Fe (modeled by the Reg_- function sensing C). Limiting mitochondrial Fe import throughout the standard Fe concentration range also required this product Reg_- function.

Cells grown on low $[\text{Fe}_{\text{med}}]$ exhibited more $F2$ than could be simulated without also generating too much $F2$ (and too little $F3$) for cells grown on high $[\text{Fe}_{\text{med}}]$. This suggested that k_{23} , the apparent rate-constant associated with the $F2 \rightarrow F3$ reaction, might increase at high $[\text{Fe}]_{\text{med}}$, perhaps reflecting more oxidized vacuoles under these conditions. To recreate this behavior, we augmented k_{23} with a $\text{Reg}_+(C, K_{32}, n32)$ function. This completes the development of the model, defined by ODEs [1] – [5].

$$\begin{aligned} \frac{d[C]}{dt} = & k_{in} \left(\frac{1}{1 + \left(\frac{[C]}{K_c}\right)^{nc}} \right) \cdot \text{nut} - k_m \left(\frac{1}{1 + \left(\frac{[C]}{K_{m1}}\right)^{nm1}} \right) \cdot \\ & \left(\frac{1}{1 + \left(\frac{[M]}{K_{m2}}\right)^{nm2}} \right) \cdot [C] - k_{cc1} \cdot \\ & \left(1 - \frac{1}{1 + \left(\frac{[C]}{K_{v1}}\right)^{nv1}} \right) \left(\frac{1}{1 + \left(\frac{[F3]}{K_{v2}}\right)^{nv2}} \right) \cdot [C] \\ & - \alpha \cdot [C] \end{aligned} \quad (1)$$

$$\frac{d[M]}{dt} = k_m \left(\frac{1}{1 + \left(\frac{[C]}{K_{m1}} \right)^{nm1}} \right) \left(\frac{1}{1 + \left(\frac{[M]}{K_{m2}} \right)^{nm2}} \right) \cdot [C] - \alpha \cdot [M] \quad (2)$$

$$\frac{d[F2]}{dt} = k_{ccc1} \left(1 - \frac{1}{1 + \left(\frac{[C]}{K_{v1}} \right)^{nv1}} \right) \left(\frac{1}{1 + \left(\frac{[F3]}{K_{v2}} \right)^{nv2}} \right) \cdot [C] - k_{23} \left(1 - \frac{1}{1 + \left(\frac{[C]}{K_{32}} \right)^{n32}} \right) \cdot [F2] - \alpha \cdot [F2] \quad (3)$$

$$\frac{d[F3]}{dt} = k_{23} \left(1 - \frac{1}{1 + \left(\frac{[C]}{K_{32}} \right)^{n32}} \right) \cdot [F2] - k_{np} [F3(t)] - \alpha \cdot [F3] \quad (4)$$

$$\frac{d[P]}{dt} = k_{np} [F3(t)] - \alpha \cdot [P] \quad (5)$$

The Fe concentration in the medium, including both added and endogenous sources, was designated by the *nut* parameter. The endogenous Fe concentration was considered to be 6 μ M. Thus, batches of cells grown with, for example, 1 and 10 μ M Fe added were simulated using *nut* = 7 and 16 μ M, respectively. For BPS-treated medium, *nut* was assumed to equal 4 μ M.

Each batch of cells used in fitting was harvested toward the end of exponential growth (doubling time \sim 2 h). Park et al. found that the concentration of Fe in exponentially growing cells is approximately invariant (i.e., $d[Fe_{cell}]/dt \approx 0$),²⁷ which implies that the sum of ODEs [1] – [5] should equal zero under these conditions. Assuming this afforded the relationship

$$k_m \left(\frac{1}{1 + \left(\frac{C(t)}{K_c} \right)^{nc}} \right) \cdot nut = \alpha \cdot [Fe_{cell}]$$

The Reg₋ valve should be largely opened (i.e., equal to \sim 1) for cells grown in Fe-deficient medium (e.g., BPS-treated). Under these conditions, $[Fe_{cell}] \sim 125 \mu$ M. This suggests $k_m \approx 16 \text{ h}^{-1}$. This equation implies that in the absence of regulation, WT cells grown on e.g. 1 mM Fe would contain \sim 30 mM Fe! Actual cells grown under such conditions contain \sim 0.5 mM Fe which illustrates the critical need for regulation in the model.

Each data set consisted of $[Fe_{cell}]$, $[M]$, $[F3]$, $[P]$, and $\{[C]+[F2]\}$ (the two components could not be separated), as determined for harvested batches of WT, $\Delta CCC1$, and *CCC1-up* cells. Data for WT W303-1B cells grown in MM containing 0 \rightarrow 10,000 μ M added Fe (the “0” refers to BPS-treated)^{8,25} were included in fitting. WT1 and WT40 cells were prepared using the DY150 strain. Data for $\Delta CCC1$ cells included batches grown on 1, 10, 20, and 40 μ M Fe. Data for *CCC1-up* cells (in normal MM) included those grown on 1, 10, 20, and 40 μ M Fe. Data for *CCC1-up* cells in MM supplemented with twice the normal concentration of adenine were also included.

The next step was to numerically integrate ODEs [1] – [5], determine $[C]$, $[M]$, $[F2]$, $[F3]$, and $[P]$ at long times when these concentrations ceased changing, and compare these simulated concentrations to those observed in actual cells. The final model included 18 free parameters, namely k_{in} , K_c , nc , k_m , K_{m1} , $nm1$, K_{m2} , $nm2$, k_{ccc1} , K_{v1} , nmv , K_{v2} , $nv2$, k_{23} , K_{32} , $n32$, k_{np} , and α . Each had to be specified before the ODEs could be integrated. To do this, we estimated values, numerically integrated the equations using Maple 17 (www.Maplesoft.com) and compared the resulting simulations to the 19 data sets just described. Parameter values were then iteratively changed to diminish differences between simulations and data.

Parameters were divided into one group that should be common to all genetic strains examined and another group that should be (or were found to be) different for each genetic strain. Common parameters included K_c , nc , K_{m1} , $nm1$, K_{m2} , $nm2$, K_{v1} , $nv1$, K_{v2} , $nv2$, k_{in} , k_m , and α (minor differences in growth rates were ignored). Strain-dependent parameters included k_{ccc1} , k_{23} , k_{np} , K_{32} , and $n32$.

An RMSD error function was developed

$$\text{RMSD} = \frac{1}{19} \sum_{j=\text{WT1, WT40...}} \sqrt{\frac{1}{4} \sum_{i=\text{F3, M...}} \left(\frac{[D_{ji}] - [S_{ji}]}{[Fe_{cell} \text{ } ji]} \right)^2}$$

in which residuals between data $[D_{ji}]$ and simulations $[S_{ji}]$ were normalized by the observed $[Fe_{cell}]$ for the particular batch j considered. These values were summed for each of the 4 experimentally distinguishable components of Fe in the cell ($i = \text{F3, M, C+F2, P}$) and for each of the 19 batches examined (76 comparisons overall). Once RMSD was approximately minimized (by manually adjusting each parameter), each parameter was increased and decreased one-at-a-time while all others were fixed. The resulting optimized values are given in Figure 8 legend. The parameter-space for such an under-determined system was too large to be explored systematically. Our final parameter set is not unique in a mathematical sense, and objectively defined uncertainties for each parameter could not be obtained. Nevertheless, we were unable to identify another parameter set that generated comparable fits despite examining >100 combinations.

Modeling Results. The model captured the essential behavior of Fe trafficking in yeast cells. The simulated total Fe concentration of each strain/condition ($[Fe_{cell}]$, top panel lines in Figure 8 and selected entries in Table S3) semi-quantitatively mimicked that of real cells grown under equivalent conditions. At $[Fe_{med}] = 40 \mu$ M, RMSDs in $[Fe_{cell}]$ were 4% for the two WT strains, 19% for $\Delta CCC1$, and 26% for *CCC1-up*. Simulated $[Fe_{cell}]$ in $\Delta CCC1$ cells was ca. 30%-less than that in WT cells, comparable to what is observed. At high $[Fe_{med}]$, the simulated $[Fe_{cell}]$ of *CCC1-up* cells was 2–8 times higher than of WT cells, also similar to that observed in real cells.

As $[Fe_{med}]$ increased, the simulated $[Fe_{cell}]$ in WT cells increased only slightly, as observed. This attenuated increase was due to the Reg₋(C , $K_c = 21$, $nc = 5$) function responding to changes in $[C]$. As $[Fe_{med}]$ increased, $[C]$ increased which caused Reg₋ to restrict Fe import. The same regulatory system was operational in all strains, including *CCC1-up* where $[Fe_{cell}]$ increased strongly with increases in $[Fe_{med}]$. Here, $[C]$ was sufficiently low such that Reg₋ did not restrict Fe import as severely as it did in other strains in which $[C]$ was higher. The decline in $[Fe_{cell}]$ of $\Delta CCC1$ cells relative to in WT cells largely

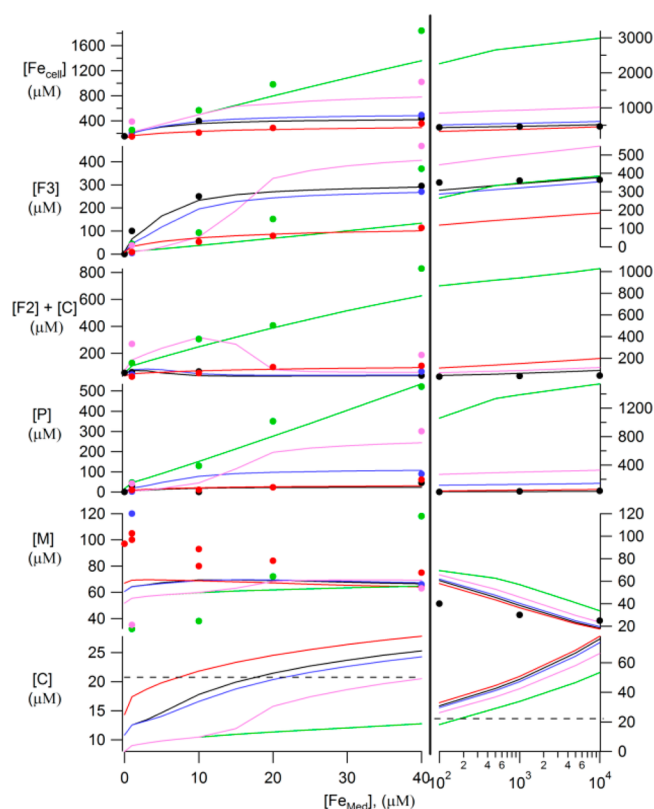


Figure 8. Simulation of iron-containing species in WT(W303) (black), WT(DY150) (blue), $\Delta ccc1$ (red), *CCC1-up* (green), and *CCC1-up* plus adenine (pink) cells at different concentration of FC in minimal medium. Solid lines are simulations for a particular strain/condition. Circles are data with the same color-coding. The dashed lines indicate the threshold concentration for cytosolic Fe. Parameters used in all simulations: $k_m = 16 \text{ h}^{-1}$; $k_{m2} = 4 \text{ h}^{-1}$; $\alpha = 0.5 \text{ h}^{-1}$; $K_c = 21 \text{ } \mu\text{M}$; $n_c = 5$; $K_{m1} = 24 \text{ } \mu\text{M}$; $n_{m1} = 3$; $K_{m2} = 90 \text{ } \mu\text{M}$; $n_{m2} = 3$; $K_{v1} = 17 \text{ } \mu\text{M}$; $n_{v1} = 6$; $K_{v2} = 200 \text{ } \mu\text{M}$; $n_{v2} = 4$. Parameters specific for the following strains, including k_{ccc1} (h^{-1}), k_{23} (h^{-1}), K_{32} (μM), n_{32} , and k_{up} (h^{-1}): WT(W303), 38, 16, 18, 9, and 0.04; WT(DY150), 38, 13, 18, 9, and 0.2; $\Delta ccc1$, 4, 1, 16, 9, and 0.15; *CCC1-up*, 400, 1, 12, 3, and 2; *CCC1-up* + adenine, 400, 9, 16, 9, and 0.3. Specific simulation and data values, along with residuals, are given in Table S3.

arose because $[C]$ in $\Delta ccc1$ cells was just slightly elevated relative to in WT cells; nevertheless, this shift was enough to slow Fe import. The absolute strain-to-strain differences in $[C]$ were amazingly small, with $[C] = 28 \text{ } \mu\text{M}$ in $\Delta ccc1$, $24 \text{ } \mu\text{M}$ in WT, and $17 \text{ } \mu\text{M}$ in *CCC1-up* cells (values quoted at $[\text{Fe}_{\text{med}}] = 40 \text{ } \mu\text{M}$). However, these small differences had a major impact on cellular Fe levels because they hovered around the threshold concentration of the Reg_- system (Figure 8, bottom panel, dashed line).

In simulations, vacuoles did not import much Fe at low $[\text{Fe}_{\text{med}}]$ (BPS-treated and $1 \text{ } \mu\text{M}$ FC conditions) but then strongly increased vacuolar flow as $[\text{Fe}_{\text{med}}]$ increased from $5 \rightarrow 30 \text{ } \mu\text{M}$, as observed. At even higher $[\text{Fe}_{\text{med}}]$, F3 levels plateaued, also as observed. This complex behavior was due to the response of the $\{\text{Reg}_+(C, K_{v1}=17, n_{v1}=6) \cdot \text{Reg}_-(F3, K_{v2}=200, n_{v2}=4)\}$ product function to changes in both $[C]$ and $[F3]$.

Simulated mitochondrial Fe concentrations $[M]$ mimicked the data adequately (Figure 8 and Table S3), but the model could not capture all strain-dependent differences. In real WT and $\Delta ccc1$ cells, $[M]$ maximized when $[\text{Fe}_{\text{med}}] \sim 1 \text{ } \mu\text{M}$; then it

plateaued and declined modestly as $[\text{Fe}_{\text{med}}]$ increased. In real *CCC1-up* cells, $[M]$ maximized later, at $[\text{Fe}_{\text{med}}] \sim 40 \text{ } \mu\text{M}$. These subtle effects were not replicated by the model. Rather, simulated $[M]$ showed a general increase, followed by a plateau and slight decline as $[\text{Fe}_{\text{med}}]$ increased. Observed levels of nanoparticle Fe $[P]$ were roughly reproduced by the model.

Unexpectedly, the high concentration of Fe in *CCC1-up* cells was *not* primarily due to the greater rate of vacuolar Fe import. One important factor was the more rapid rate of nanoparticle formation (k_{np} was 10–50 times faster in *CCC1-up* cells than in WT cells and 13 times faster than in $\Delta ccc1$ cells). Nanoparticles probably formed more rapidly in *CCC1-up* cells because the vacuoles are more basic than they are in WT or $\Delta ccc1$ cells. This may be due to the extra *Ccc1p* that pumps protons out of the vacuole as it imports Fe and other metal ions.⁴⁶ This effect was diminished in the UP+A cells (k_{np} was 7 times slower in UP+A cells than in UP cells), explaining the $4 \rightarrow 9$ fold decline in overall Fe concentration.

According to simulations, another factor causing *CCC1-up* cells to load with Fe is that they contained almost 7-times more F2 than $\Delta ccc1$ cells and 50-times more than WT cells (at $[\text{Fe}_{\text{med}}] = 40 \text{ } \mu\text{M}$). In our model, vacuolar Fe import was sensitive to $[F3]$ rather than to $[F2]$ such that high $[F2]$ did not trigger shutdown of vacuolar Fe import. Given the high concentrations of F2, *CCC1-up* vacuoles (like $\Delta ccc1$ vacuoles) may be more reducing than WT vacuoles. Relieving the adenine deficiency of these cells involved making the vacuoles more oxidizing.

DISCUSSION

Understanding the trafficking and regulation of iron in eukaryotic cells is complicated by the large numbers and incompletely defined components and reactions involved. The reductionist approach of isolating, identifying, and characterizing individual components is clearly required to understand these high-level processes. However, perceiving how these components function together to give rise to cellular Fe trafficking and regulation is also required; this involves a systems-level approach.

Systems-level studies of Fe trafficking and regulation in cells generally involve characterizing the phenotype associated with various genotypes. This is essentially the approach used here, except that our characterization involved biophysical methods that are not usually employed in genetic studies. Two genetic strains of yeast were studied in which the gene encoding the only known Fe import protein into vacuoles (*CCC1*) was either deleted or overexpressed. We applied Mössbauer, EPR, and UV-visible spectroscopies to explore the phenotype of these strains from an iron-centric perspective. We measured the absolute Fe concentration in these cells and decomposed that Fe into various groups. These groups included a mononuclear HS Fe^{III} species located in vacuoles, ISC's and NHHS Fe^{II} species and nanoparticles the locations of which are less certain, but probably cytosolic or vacuolar. We also developed a simple mathematical model that described Fe trafficking and regulation in yeast. For each genetic strain, the model simulated how the concentrations of these groups of Fe changed with changes in $[\text{Fe}_{\text{med}}]$. Combining experimental and computational approaches allowed a synergistic interplay that would not have been possible had only one approach been taken. Due to unknowns in regulation, we employed the surrogate Reg_{\mp} functions in our model to regulate the import of cellular Fe

at the plasma membrane, the import of cytosolic Fe into vacuoles and mitochondria, and the conversion of Fe^{II} to Fe^{III}. With these Reg functions included, our model captured essential features of Fe regulation in yeast cells. As the molecular-level details of Fe regulation become known, these Reg functions can be replaced by molecular-level mechanisms.

According to our model, the import of nutrient Fe through the plasma membrane is regulated by sensing the concentration of the cytosolic species *C* that results from the importation. This is the same species that is imported into vacuoles and mitochondria in subsequent steps. The threshold concentration was 21 μ M, and $[C]$ remained near to this value for all genetic strains, and for all “normal” nutrient Fe concentrations (1–100 μ M). As predicted by Kaplan, $[C]$ was higher in $\Delta ccc1$ cells and lower in *CCC1-up* cells, relative to the analogous concentration in WT cells.

Unexpectedly, our model suggests that the strain-dependent differences in $[C]$ are quite small. The entire system responds to the blockage/enhancement of entry into vacuoles by moderating these perturbations. We initially thought that the entire NHHS Fe^{II} species observed in $\Delta ccc1$ cells was *C*. But if this were the case, Fe import would have been virtually shut-down (because the concentration of the species was so high relative to threshold). In reality, additional Fe enters $\Delta ccc1$ cells grown at higher $[Fe]_{med}$. This implies that a portion of the NHHS Fe^{II} in $\Delta ccc1$ cells originates from another species (*F2*) that is not sensed by the Fe import regulatory system. Indeed, simulations strongly suggest that the bulk of the observed NHHS Fe^{II} species in $\Delta ccc1$ cells arose from *F2*, not *C*. *This situation highlights the critical importance of quantitative modeling in evaluating Fe trafficking hypotheses.*

Our results suggest (but do not prove) that *C* is a mononuclear NHHS Fe^{II} species—either protein-associated or part of a low-molecular-mass complex. We find this possibility appealing because the coordination environment of such Fe complexes tend to be labile, as might be important for a trafficking complex that is also sensed for regulation. Also, these same types of NHHS Fe^{II} complexes would also be expected to participate in Fenton chemistry and to be associated with increased ROS damage. Our conclusion is not definitive because most of the NHHS Fe^{II} species in $\Delta ccc1$ and *CCC1-up* cells appears to arise from species other than *C*. Thus, we cannot exclude the possibility that *C* is a completely different species that has not been detected or identified. For example, *C* could be an $[Fe_2S_2]$ cluster, perhaps associated with Grx3/4, Fra2p, and/or Aft1p.³³ In cells containing 200–500 μ M Fe, such minor species (with a concentration of *ca.* 20 μ M or less) would be difficult to detect by our biophysical methods.

The dominating portion of NHHS Fe^{II} that we observe in these strains probably arises from the reduction of vacuolar Fe^{III}. The concentration of such species (labeled *F2* in our model) probably reflects the redox status of vacuoles, with vacuoles of $\Delta ccc1$ and *CCC1-up* cells more reducing than those in WT cells. We suspect that the nanoparticles present in the mutant strains are derived from vacuolar Fe^{III} in which the pH of the organelle is higher than normal. Many of the effects observed in this study probably arise from alterations of Fe in the vacuoles, due ultimately to the absence or abundance of Ccc1p. The magnitude of k_{23} is related to the oxidation state of the vacuoles, with faster rates indicating more oxidizing conditions. The magnitude of k_{np} is related to the pH of the vacuole, with faster rates associated with more basic conditions.

We hypothesize that the vacuolar pH is higher in UP40 cells than in WT cells. The vacuolar pH could have increased as a result of exporting H⁺ during Ccc1p-mediated Fe^{II} import.^{4,47}

Our finding that DY150 cells showed higher ratios of nanoparticles/NHHS Fe^{III} than W303-1B cells suggests that the pH of vacuoles in DY150 cells is slightly higher than in W303-1B vacuoles. The similar overall Fe concentration in both strains indicates that nanoparticle formation was not due to increased Fe uptake but to a shift in the distribution of Fe.

Adding excess adenine to UP40 cells resulted in less NHHS Fe^{II} and more nanoparticles. Nanoparticle formation is favored under oxidizing and high pH conditions. This would suggest that adenine deficiency leads to a more reducing vacuolar environment, supporting the recent results of Park and Lindahl (unpublished).

Overall, our results provide new insights into the Fe metabolism of vacuoles, the organelles that store and sequester Fe. The Fe in vacuoles is not “fixed” in the commonly observed HS Fe^{III} state but rather is sensitive to the oxidation status and pH of the organelle. Under reducing conditions, vacuolar Fe^{III} is reduced to Fe^{II}. Under basic conditions, vacuolar Fe^{III} is converted into nanoparticles. Whether reduction involves ligand-exchange and/or movement out of the vacuole is unknown. Nanoparticle formation does not involve redox changes of the Fe^{III} ion but it must involve changes in its coordination environment (development of bridging ligands) such that mononuclear Fe^{III} complexes aggregate and magnetically interact.

Limitations of the Model. Highlighting the deficiencies of the model is as important as highlighting its strengths. The model is simplistic and ignores many aspects of cellular Fe metabolism and regulation; we plan to develop more sophisticated models in the future, especially with regard to processes occurring in mitochondria. The model did not simulate a decline in mitochondrial Fe with increasing medium Fe. Kaplan and others have reported “cross-talk” between vacuoles and mitochondria,^{20,47,48} and these effects need to be included. The volumes of cytosol and various organelles should also be included, and more sophisticated methods for optimization and sensitivity analysis should be developed.

Manganese. Although not the focus of this paper, we discovered new aspects of Mn metabolism that relate indirectly to the effects of Ccc1p on Fe metabolism. Ccc1p also imports cytosolic Mn to the vacuole.³¹ We found that the concentration of Mn in the cell varied with genetic strain. $\Delta ccc1$ cells contained half the Mn concentration of WT cells, and WT cells contained half the Mn concentration of *CCC1-up* cells. Arguing as we have done for Fe, deleting *CCC1* probably increases cytosolic Mn which lowers the rate of cellular Mn import. Overexpressing *CCC1* increases Mn import into the vacuole, creating a deficiency in the cytosol which increases cellular Mn import. This suggests a regulatory mechanism for Mn import functionally similar to that described here for Fe, sensing cytosolic (not vacuolar) Mn. We have quantified these ideas via a mathematical model similar to that used here to study Fe trafficking (see Supporting Information). Optimized simulated concentrations for $[Mn_{cell}]$ in $\Delta ccc1$, WT, and *CCC1-up* strains were 16, 34, and 76 μ M, respectively, which are very similar to experimental values (Table S2). According to the model, 83%, 33%, and 5% of the Mn in these 3 strains were cytosolic, respectively, with the remainder present in vacuoles. The threshold concentration of cytosolic Mn was 11 μ M. About 90% of Mn in the cell was EPR-active, indicating a dominance

of mononuclear Mn^{II} complexes. McNaughton et al. have probed the speciation of Mn in yeast cells using ENDOR spectroscopy.⁴⁹ They found that in WT cells, ~75% of cellular Mn was EPR-active, similar to that determined here. Their WT cells contained 26 μM Mn, with about half of that present as a low-molecular-mass Mn^{II} complex with aqua and phosphate ligands. Another quarter was present as a similar complex but with polyphosphate ligands. Given the dominance of polyphosphate ligands in the vacuole,^{7,47} we hypothesize that the polyphosphate Mn^{II} complex is located in vacuoles while the phosphate-coordinated complex is cytosolic. Our previous conclusion that little Mn was present in vacuoles⁹ was based on studies using isolated vacuoles, which contained low concentrations of Mn ($1.7 \pm 0.6 \mu M$) and the low spin concentrations of the Mn-based EPR signal. The Fe concentration in isolated vacuoles was also low ($220 \pm 100 \mu M$) relative to that present in vacuoles contained in whole cells (estimated at 1.2 mM). This situation probably arises from the rapid import:export dynamics expected for an organelle that stores and delivers metal ions to the cytosol as needed. We suspect that the concentration of Mn in vacuoles present in WT cells (grown on MM) is proportionately higher – e.g. 6–10 μM – similar to the concentration calculated for the polyphosphate-coordinated complex in the ENDOR study. Our model predicts that Ccc1p imports Fe^{II} ca. 40× faster than it does Mn^{II}.

■ ASSOCIATED CONTENT

■ Supporting Information

Strain verification of *CCC1-up* (Western blot) and $\Delta ccc1$ (Figure S1), Oxyblot of whole cell extracts (Figure S2), electronic absorption spectrum of mitochondria from $\Delta 40$ cells (Figure S3), MB spectrum of vacuoles isolated from UP40 cells (Figure S4), MB spectrum of vacuoles isolated from UP40 cells (Figure S5), EPR of UP40 + A cells (Figure S6), quantifications of heme centers found by UV–vis (Table S1), Fe and Mn concentrations and EPR intensities (Table S2), simulations, data and residuals for Fe models (Table S3), and the mathematical model of Mn trafficking in yeast. This material is available free of charge via the Internet at <http://pubs.acs.org>.

■ AUTHOR INFORMATION

Corresponding Author

*Phone: 979-845-0956. E-mail: Lindahl@chem.tamu.edu.

Author Contributions

A.C. designed, performed and analyzed most of the experiments and wrote major portions of the paper. S.P.M. performed the ICP-MS experiments, M.M. isolated mitochondria, M.C. maintained the MB spectrometers and helped collect and analyze the MB and EPR data. P.A.L. helped design and analyze the experiments, wrote the mathematical model, and wrote and edited the paper. All authors approved the final version of the manuscript.

Funding

This study was funded by the National Institutes of Health (GM084266), the Robert A. Welch Foundation (A1170), and the National Science Foundation (DMS-0714896).

Notes

The authors declare no competing financial interest.

■ ACKNOWLEDGMENTS

We thank Dr. Jerry Kaplan (University of Utah) for generously providing the yeast strains and Ccc1p antibody used in this

study and for helpful discussions. We also thank Roland Lill, Philipps Universität, Marburg Germany for providing the W303-1B strain, and Brad Pierce, University of Texas at Arlington, for allowing us to use his EPR spectrometer.

■ ABBREVIATIONS

BPS, bathophenanthroline sulfonate; C, model component symbolizing cytosolic Fe; *CCC1*, gene encoding the Ccc1 protein; $\Delta ccc1$, yeast strain with *CCC1* deleted; *CCC1-up*, yeast strain with *CCC1* overexpressed; CD, central quadrupole doublet; δ , isomer shift; DDDI, double-distilled and deionized; $\Delta 1$, $\Delta 10$, $\Delta 20$, and $\Delta 40$, $\Delta ccc1$ cells grown on MM containing 1, 10, 20, and 40 μM FC, respectively; EPR, electron paramagnetic resonance; F2, model component symbolizing NHHS Fe^{II}; F3, model component symbolizing NHHS Fe^{III}; $[Fe_{cell}]$, concentration of Fe in the cell; $[Fe_{med}]$, concentration of FC added to MM; FC, ferric citrate; ICP-MS, inductively coupled plasma mass spectrometry; M, model component symbolizing mitochondrial Fe; MB, Mössbauer; MM, minimal medium; NHHS, nonheme high-spin; ODE, ordinary differential equation; P, model component symbolizing Fe^{III} phosphate/polyphosphate associated nanoparticles; ΔE_Q , quadrupole splitting; RMSD, root-mean-square deviation; ROS, reactive oxygen species; UP1, UP10, UP20, and UP40, *CCC1-up* cells grown on MM containing 1, 10, 20, and 40 μM FC, respectively; UP1+A and UP40+A, *CCC1-up* cells grown on MM containing twice the normal concentration of adenine, along with 1 and 40 μM FC, respectively; WT1, WT40, wild-type cells grown in MM containing 1 and 40 μM FC, respectively

■ REFERENCES

- (1) Crichton, R. R., and Pierre, J. L. (2001) Old iron, young copper: From Mars to Venus. *Biometals* 14, 99–112.
- (2) Flint, D. H., and Allen, R. M. (1996) Iron-sulfur proteins with nonredox functions. *Chem. Rev.* 96, 2315–2334.
- (3) Lill, R., Hoffmann, B., Molik, S., Pierik, A. J., Rietzschel, N., Stehling, O., Uzarska, M. A., Weber, H., Wilbrecht, C., and Mühlenhoff, U. (2012) The role of mitochondria in cellular iron-sulfur protein biogenesis and iron metabolism. *Biochim. Biophys. Acta* 1823, 1491–1508.
- (4) Li, L. T., Chen, O. S., Ward, D. M., and Kaplan, J. (2001) CCC1 is a transporter that mediates vacuolar iron storage in yeast. *J. Biol. Chem.* 276, 29515–29519.
- (5) Urbanowski, J. L., and Piper, R. C. (1999) The iron transporter *fth1p* forms a complex with the Fet5 iron oxidase and resides on the vacuolar membrane. *J. Biol. Chem.* 274, 38061–38070.
- (6) Portnoy, M. E., Liu, X. F., and Culotta, V. C. (2000) *Saccharomyces cerevisiae* expresses three functionally distinct homologues of the Nramp family of metal transporters. *Mol. Cell. Biol.* 20, 7893–7902.
- (7) Singh, A., Kaur, N., and Kosman, D. J. (2007) The metalloredox Fre6p in Fe-Efflux from the yeast vacuole. *J. Biol. Chem.* 282, 28619–28626.
- (8) Holmes-Hampton, G. P., Jhurry, N. D., McCormick, S. P., and Lindahl, P. A. (2013) Iron content of *Saccharomyces cerevisiae* cells grown under iron-deficient and iron-overload conditions. *Biochemistry* 52, 105–114.
- (9) Cockrell, A. L., Holmes-Hampton, G. P., McCormick, S. P., Chakrabarti, M., and Lindahl, P. A. (2011) Mössbauer and EPR study of iron in vacuoles from fermenting *Saccharomyces cerevisiae*. *Biochemistry* 50, 10275–10283.
- (10) Shvartsman, M., and Cabantchik, Z. I. (2012) Intracellular iron trafficking: role of cytosolic ligands. *Biometals* 25, 711–723.

- (11) Li, L., Bagley, D., Ward, D. A., and Kaplan, J. (2008) Yap5 is an iron-responsive transcriptional activator that regulates vacuolar iron storage in yeast. *Mol. Cell. Biol.* 28, 1326–1337.
- (12) Puig, S., Askeland, E., and Thiele, D. J. (2005) Coordinated remodeling of cellular metabolism during iron deficiency through targeted mRNA degradation. *Cell* 120, 99–110.
- (13) Kaplan, C. D., and Kaplan, J. (2009) Iron Acquisition and Transcriptional Regulation. *Chem. Rev.* 109, 4536–4552.
- (14) Askwith, C., Eide, D., Vanho, A., Bernard, P. S., Li, L. T., DavisKaplan, S., Sipe, D. M., and Kaplan, J. (1994) The Fet3 Gene of *Saccharomyces cerevisiae* Encodes a Multicopper Oxidase Required for Ferrous Iron Uptake. *Cell* 76, 403–410.
- (15) Spizzo, T., Byersdorfer, C., Duesterhoeft, S., and Eide, D. (1997) The yeast FET5 gene encodes a FET3-related multicopper oxidase implicated in iron transport. *Mol. Gen. Genet.* 256, 547–556.
- (16) Desilva, D. M., Askwith, C. C., Eide, D., and Kaplan, J. (1995) The Fet3 Gene-Product Required for High-Affinity Iron Transport in Yeast Is a Cell-Surface Ferroxidase. *J. Biol. Chem.* 270, 1098–1101.
- (17) Philpott, C. C., and Protchenko, O. (2008) Response to iron deprivation in *Saccharomyces cerevisiae*. *Eukaryotic Cell* 7, 20–27.
- (18) Cohen, A., Nelson, H., and Nelson, N. (2000) The family of SMF metal ion transporters in yeast cells. *J. Biol. Chem.* 275, 33388–33394.
- (19) Philpott, C. C. (2012) Coming into view: eukaryotic iron chaperones and intracellular iron delivery. *J. Biol. Chem.* 287, 13518–13523.
- (20) Li, L. T., and Kaplan, J. (2004) A mitochondrial-vacuolar signaling pathway in yeast that affects iron and copper metabolism. *J. Biol. Chem.* 279, 33653–33661.
- (21) Foury, F., and Roganti, T. (2002) Deletion of the mitochondrial carrier genes MRS3 and MRS4 suppresses mitochondrial iron accumulation in a yeast frataxin-deficient strain. *J. Biol. Chem.* 277, 24475–24483.
- (22) Lindahl, P. A., Morales, J. G., Miao, R., and Holmes-Hampton, G. (2009) Isolation of *Saccharomyces cerevisiae* Mitochondria for Mössbauer, EPR, and Electronic Absorption Spectroscopic Analyses. *Method Enzymol.* 456, 267–285.
- (23) Morales, J. G., Holmes-Hampton, G. P., Miao, R., Guo, Y. S., Münck, E., and Lindahl, P. A. (2010) Biophysical Characterization of Iron in Mitochondria Isolated from Respiring and Fermenting Yeast. *Biochemistry* 49, 5436–5444.
- (24) Orme-Johnson, N. R., and Orme-Johnson, W. H. (1978) Detection and quantitation of free cytochrome P-450 and cytochrome P-450 complexes by EPR spectroscopy. *Methods Enzymol.* 52, 252–257.
- (25) Miao, R., Holmes-Hampton, G., and Lindahl, P. A. (2011) Biophysical Investigation of the Iron in Aft1–Iup and Gal-YAH1 *Saccharomyces cerevisiae*. *Biochemistry* 50, 2660–2671.
- (26) Holmes-Hampton, G. P., Miao, R., Morales, J. G., Guo, Y. S., Münck, E., and Lindahl, P. A. (2010) A Nonheme High-Spin Ferrous Pool in Mitochondria Isolated from Fermenting *Saccharomyces cerevisiae*. *Biochemistry* 49, 4227–4234.
- (27) Park, J., McCormick, S. P., Chakrabarti, M., and Lindahl, P. A. (2013) The lack of synchronization between iron uptake and cell growth leads to iron overload in *Saccharomyces cerevisiae* during post-exponential growth modes. *Biochemistry* 52, 9413–9425.
- (28) Miao, R., Kim, H., Koppolu, U. M. K., Ellis, E. A., Scott, R. A., and Lindahl, P. A. (2009) Biophysical Characterization of the Iron in Mitochondria from Atm1p-Depleted *Saccharomyces cerevisiae*. *Biochemistry* 48, 9556–9568.
- (29) Miao, R., Martinho, M., Morales, J. G., Kim, H., Ellis, E. A., Lill, R., Hendrich, M. P., Münck, E., and Lindahl, P. A. (2008) EPR and Mössbauer spectroscopy of intact mitochondria isolated from Yah1p-depleted *Saccharomyces cerevisiae*. *Biochemistry* 47, 9888–9899.
- (30) Sharma, K. G., Kaur, R., and Bachhawat, A. K. (2003) The glutathione-mediated detoxification pathway in yeast: an analysis using the red pigment that accumulates in certain adenine biosynthetic mutants of yeasts reveals the involvement of novel genes. *Arch. Microbiol.* 180, 108–117.
- (31) Lapinskas, P. J., Lin, S. J., and Culotta, V. C. (1996) The role of the *Saccharomyces cerevisiae* CCC1 gene in the homeostasis of manganese ions. *Mol. Microbiol.* 21, 519–528.
- (32) Outten, C. E., and Albetel, A. N. (2013) Iron sensing and regulation in *Saccharomyces cerevisiae*: ironing out the mechanistic details. *Curr. Opin. Microbiol.* 16, 662–668.
- (33) Li, H., Mapolelo, D. T., Dingra, N. N., Naik, S. G., Lees, N. S., Hoffman, B. M., Riggs-Gelasco, P. J., Huynh, B. H., Johnson, M. K., and Outten, C. E. (2009) The yeast iron regulatory proteins Grx3/4 and Fra2 form heterodimeric complexes containing a [2Fe-2S] cluster with cysteinyl and histidyl ligation. *Biochemistry* 48, 9569–9581.
- (34) Li, H. R., Mapolelo, D. T., Dingra, N. N., Keller, G., Riggs-Gelasco, P. J., Winge, D. R., Johnson, M. K., and Outten, C. E. (2011) *J. Biol. Chem.* 286, 867–876.
- (35) Yamaguchi-Iwai, Y., Dancis, A., and Klausner, R. D. (1995) AFT1: a mediator of iron regulated transcriptional control in *Saccharomyces cerevisiae*. *EMBO J.* 14, 1231–1239.
- (36) Ueta, R., Fujiwara, N., Iwai, K., and Yamaguchi-Iwai, Y. (2012) Iron-induced dissociation of the Aft1p transcriptional regulator from target gene promoters is an initial event in iron-dependent gene suppression. *Mol. Cell. Biol.* 32, 4998–5008.
- (37) Li, L., Miao, R., Bertram, S., Jia, X., Ward, D. M., and Kaplan, J. (2012) A role for iron-sulfur clusters in the regulation of transcription factor Yap5-dependent high iron transcriptional responses in yeast. *J. Biol. Chem.* 287, 35709–35721.
- (38) Pimentel, C., Vicente, C., Menezes, R. A., Caetano, S., Carreto, L., and Rodrigues-Pousada, C. (2012) The role of the Yap5 transcription factor in remodeling gene expression in response to Fe bioavailability. *PLoS One* 7, e37434.
- (39) Martinez-Pastor, M., Vergara, S. V., Puig, S., and Thiele, D. J. (2013) Negative feedback regulation of the yeast CTH1 and CTH2 mRNA binding proteins is required for adaptation to iron deficiency and iron supplementation. *Mol. Cell. Biol.* 33, 2178–2187.
- (40) Mühlenhoff, U., Stadler, J. A., Richhardt, N., Seubert, A., Eickhorst, T., Schweyen, R. J., Lill, R., and Wiesenberger, G. (2003) A specific role of the yeast mitochondrial carriers MRS3/4p in mitochondrial iron acquisition under iron-limiting conditions. *J. Biol. Chem.* 278, 40612–40620.
- (41) Froschauer, E. M., Schweyen, R. J., and Wiesenberger, G. (2009) The yeast mitochondrial carrier proteins Mrs3p/Mrs4p mediate iron transport across the inner mitochondrial membrane. *Biochim. Biophys. Acta* 1788, 1044–1050.
- (42) Vilella, F., Alves, R., Rodriguez-Manzanique, M. T., Belli, G., Swaminathan, S., Sunnerhagen, P., and Herrero, E. (2004) Evolution and cellular function of monothiol glutaredoxins: involvement in iron-sulphur cluster assembly. *Comp. Funct. Genomics* 5, 328–341.
- (43) Ojeda, L., Keller, G., Mühlenhoff, U., Rutherford, J. C., Lill, R., and Winge, D. R. (2006) Role of glutaredoxin-3 and glutaredoxin-4 in the iron regulation of the Aft1 transcriptional activator in *Saccharomyces cerevisiae*. *J. Biol. Chem.* 281, 17661–17669.
- (44) Pujol-Carrion, N., Belli, G., Herrero, E., Nogues, A., and de la Torre-Ruiz, M. A. (2006) Glutaredoxins Grx3 and Grx4 regulate nuclear localisation of Aft1 and the oxidative stress response in *Saccharomyces cerevisiae*. *J. Cell Sci.* 119, 4554–4564.
- (45) Kumanovics, A., Chen, O. S., Li, L., Bagley, D., Adkins, E. M., Lin, H., Dingra, N. N., Outten, C. E., Keller, G., Winge, D., Ward, D. M., and Kaplan, J. (2008) Identification of FRA1 and FRA2 as genes involved in regulating the yeast iron regulon in response to decreased mitochondrial iron-sulfur cluster synthesis. *J. Biol. Chem.* 283, 10276–10286.
- (46) Martinoia, E., Maeshima, M., and Neuhaus, H. E. (2007) Vacuolar transporters and their essential role in plant metabolism. *J. Exp. Bot.* 58, 83–102.
- (47) Raguzzini, F., Lesuisse, E., and Crichton, R. R. (1988) Iron storage in *Saccharomyces cerevisiae*. *FEBS Lett.* 231, 253–258.
- (48) Li, T. L., Murdock, G., Bagley, D., Jia, X. A., Ward, D. M., and Kaplan, J. (2010) Genetic dissection of a mitochondria-vacuole signaling pathway in yeast reveals a link between chronic oxidative stress and vacuolar iron transport. *J. Biol. Chem.* 285, 10232–10242.

(49) McNaughton, R. L., Reddi, A. R., Clement, M. H., Sharma, A., Barnese, K., Rosenfeld, L., Gralla, E. B., Valentine, J. S., Culotta, V. C., and Hoffman, B. M. (2010) Probing in vivo Mn^{2+} speciation and oxidative stress resistance in yeast cells with electron-nuclear double resonance spectroscopy. *Proc. Natl. Acad. Sci. U.S.A.* 107, 15335–15339.